Progress in Surface Science 99 (2024) 100743

Contents lists available at ScienceDirect

Progress in Surface Science

journal homepage: www.elsevier.com/locate/progsurf

Review article

Structural dynamics in atomic indium wires on silicon: From ultrafast probing to coherent vibrational control

Jan Gerrit Horstmann [a,b,*], Hannes Böckmann [b], Felix Kurtz [b], Gero Storeck [b], Claus Ropers [b,c]

[a] Department of Materials, ETH Zürich, Vladimir-Prelog-Weg 1-5/10, 8093 Zürich, Switzerland
[b] Department of Ultrafast Dynamics, Max Planck Institute for Multidisciplinary Sciences, Am Fassberg 11, 37077 Göttingen, Germany
[c] 4th Physical Institute, Georg August University of Göttingen, Friedrich-Hund-Platz 1, 37077 Göttingen, Germany

ARTICLE INFO

Commissioning Editor: Hrvoje Petek

Keywords:
Ultrafast low-energy electron diffraction
Low-dimensional strongly correlated systems
Coherent control
Mode-selective excitation
Metal-insulator transition

ABSTRACT

Light-control of structural dynamics at surfaces promises switching of chemical and physical functionality at rates limited only by the velocity of directed atomic motion. Following optical stimulus by femtosecond light pulses (1 fs = 10^{-15} s), transient electronic and lattice excitations can drive phase transitions in solids. Coherent control schemes facilitate a selective transfer of optical energy to specific electronic or vibrational degrees of freedom, as exemplified by the steering of molecular reactions via optical pulse sequences in femtochemistry. However, a transfer of this concept from molecules to solids requires coupling of few decisive phonons to optical transitions in the electronic band structure, and a weak coupling to other lattice modes to maximize coherence times. In this respect, atomic indium wires on the (111) surface of silicon represent a highly attractive model system, with a Peierls-like phase transition between insulating (8×2) and metallic (4×1) structures, governed by shear and rotation phonons. This review provides a survey on our advances in the time-resolved probing and coherent vibrational control of the In/Si(111) surface. In particular, we discuss how coherent atomic motion can be harnessed to affect the efficiency and threshold of the phase transition. Starting from a description of the (8×2) and (4×1) equilibrium structures and key vibrational modes, we study the structural dynamics following single-pulse optical excitation of the (8×2) phase. Our results highlight the ballistic order-parameter motion in the nonequilibrium transition as well as the impact of microscopic heterogeneity on the excitation and subsequent relaxation of the metastable photo-induced (4×1) phase. Furthermore, we discuss our results on the combination of ultrafast low-energy electron diffraction (ULEED) with optical pulse sequences to investigate the coherent control over the transition, mode-selective excitation and the location of the transition state.

1. Introduction

The properties of solids are governed by intricate interactions between multiple degrees of freedom, including charge, lattice, spin, orbital order, and topology. Correlations within and between these subsystems lead to emergent phenomena, such as (un-)conventional superconductivity [1–3], or correlated insulators [4,5]. Highlighting the subtle competition between different interactions in a

* Corresponding author.
E-mail address: jan-gerrit.horstmann@mat.ethz.ch (J.G. Horstmann).

https://doi.org/10.1016/j.progsurf.2024.100743

Available online 22 April 2024

crystalline solid, structural phase transformations are among the most fascinating phenomena in condensed matter science: A small change in temperature or pressure may tilt the balance and result in a structural transformation that is accompanied by often drastic changes in a material's physical properties.

Emergent phases are frequently governed by electron–electron and electron–phonon interactions and are commonly facilitated by a reduced dimensionality [6,7]. The concomitant enhancement of correlations affects both electronic and vibrational states of materials and causes new collective excitations and ground states [5,8,9]. Arguably one of the most fascinating consequences of electron–phonon coupling in low-dimensional materials is the Peierls instability, which results in the formation of charge density waves (CDWs) [10–12]. Peierls [8] and Fröhlich [13] noted that at zero temperature, a one-dimensional, equally-spaced atomic chain with one electron per ion is unstable to a periodic distortion of the lattice. Their theoretical model only received more attention when quasi-one-dimensional systems came into focus, motivated by the search for high-T_c superconductors [12]. Instead of hosting a superconducting state, some of these systems, specifically those exhibiting partially filled bands, underwent a metal–insulator transition below a critical temperature T_c, accompanied by pronounced structural changes, as predicted by Peierls and Fröhlich. Since their discovery, CDWs are among the most frequently investigated phenomena in solids, with examples in simple metals [14], transition-metal dichalcogenides [15,16] or bronzes [17,18], rare earth tellurides [19–21] as well as organic linear chain compounds [22].

The specific correlations defining the phases and transitions of a material are often difficult to disentangle in equilibrium. Therefore, sophisticated methods in ultrafast spectroscopy [23,24], diffraction [25–28], and imaging [29–31] have been developed to trace out the strengths and hierarchies of couplings in the time domain. Pump-probe techniques using electron or photon probe pulses across the spectrum have been successful in resolving the nonequilibrium evolution of structural [32–34], electronic [35–37] or spin dynamics [38–40] in materials systems promoted into highly excited states. These approaches have targeted the study of various light-induced structural phase transitions involving CDWs, aiming at the elucidation of, for example, electronic and structural origins of particular transitions [15,34,36,41]. Beyond resolving the speed of a particular known transformation, such studies have uncovered the creation of novel metastable and transient states, which are inaccessible under equilibrium conditions [42–44]. Moreover, growing abilities to follow and control the dynamic state of materials give rise to fundamental questions on structural transformations driven far from equilibrium (see Fig. 1). In the following, we highlight a select group of current overarching research questions:

1) **Coupling to the three-dimensional environment.** Although correlated phenomena are particularly pronounced in low dimensions, coupling to the three-dimensional environment is inevitable. For example, the Peierls transition is forbidden in a strictly one-dimensional system where fluctuations prevent the formation of a long-range order [10,45]. However, the transition can still occur if there is a strong enough coupling to the higher-dimensional environment. Electron diffraction studies have highlighted the role of dimensional crossovers in such systems [46]. In this context, relevant questions concern strategies to characterize and potentially tailor the effective dimensionality of materials.
2) **Novel and functional metastable states.** Nonequilibrium excitations of the electronic and structural degrees of freedom induce a dynamical evolution of a materials system, which may result in its metastable or permanent transformation. The final state of such a nonequilibrium trajectory may or may not correspond to an equilibrium phase. Specifically, it has been shown that ultrashort laser or electric current pulses can produce "hidden" metastable states [42–44] with physical properties drastically deviating from the corresponding equilibrium phase. The search for such phases and the conditions to prepare them holds promise for fundamental insights and new functionalities.

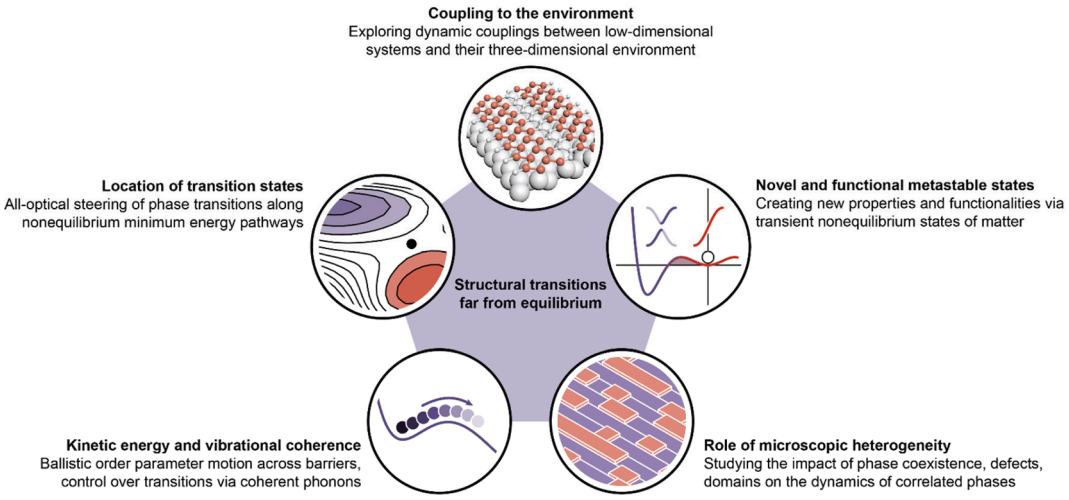

Fig. 1. Structural transformations far from equilibrium. Owing to its quasi-one-dimensional nature, its first-order metal–insulator transition, and the strong coupling of the corresponding key phonon modes to electronic excitations, the In/Si(111) surface represents a model system for essential aspects of nonequilibrium dynamics in solids. These include the coupling between low-dimensional systems and their higher-dimensional environment, metastability, microscopic heterogeneity, coherent vibrational motion and the location of transition states.

3) **Role of microscopic heterogeneity.** The functionality of materials and surfaces in particular is often defined by microscopic heterogeneity. Phase coexistence and phase boundaries, interfaces as well as adsorbates and other defects alter the local electronic and lattice structure and thus the emergence of correlated phases [29,47,48]. There is a particular challenge in both modeling as well as experimentally investigating the influence of heterogeneity in phase transformations.
4) **Kinetic energy and vibrational coherence in phase transitions.** Structural phase transitions involve the rearrangement of nuclear coordinates and a change in structural symmetries. Peierls insulators exhibit amplitude modes along the displacement between the structures of the high-symmetry and broken-symmetry phases [10,49,50]. A number of studies indicates that a coherent excitation of amplitude modes governs the barrier and dynamics of phase transformations [51–53]. More generally, the question is to what degree directed kinetic energy in specific modes can be harnessed to control the efficiencies and pathways of solid-state phase transitions.
5) **Location of transition states.** The notion of transition states is ubiquitous in the study of molecular transformations, denoting the highest-energy configuration along the reaction path. The influence of vibrational excitation on a transition is strongly affected by the location of the transition state, as expressed in the Polanyi rules [54]. Also condensed-matter systems that undergo a transformation along particular collective coordinates may exhibit well-defined transition states. Their study will yield a fundamental understanding of the multidimensional energy landscape and will provide strategies for energy-efficient functional control.

The above represents a challenging, albeit incomplete, list of exciting research directions to which ultrafast measurement technology can provide meaningful solutions. Over the past years, a number of model systems have emerged, which enable a comprehensive investigation of these complex problems by a variety of experimental techniques. Atomic indium wires on a silicon (111) surface (hereafter referred to as 'In/Si(111)') represent a particularly interesting low-dimensional system, in which many of the above phenomena can be addressed. This review aims at an introduction of the basic properties of the system, an overview of previous work, and a discussion of some of the developments in the field, with an emphasis on structural dynamics. We begin with a description of the elementary structural properties and their appearance in low-energy electron diffraction (LEED) and other techniques (Sec. 2).

2. Atomic indium wires on silicon

2.1. Peierls transition and overview of the sample system

Quasi-one-dimensional systems are particularly promising candidates for electron–phonon-correlated CDW formation, as their real-space anisotropy typically translates into a highly anisotropic electronic band structure. The corresponding Fermi surface exhibits large parallel-running sections facilitating phonon-mediated electron-hole pairing over the entire Brillouin zone. In the simplest case of a linear atomic chain with real-space lattice constant a, each atom contributes a single electron, forming a quasi-free 1D electron gas. Since each electronic state can be filled with two electrons of opposite spin, this corresponds to a half-filled band. Introducing a lattice distortion with periodicity $2a$ leads to energetically degenerate states at wavenumbers $k = \pm k_F = \pm\pi/2a$. For $T < T_c$, the coupling of electrons and holes (with opposite spins) removes this degeneracy via the formation of electronic band gaps around the Fermi energy E_F, i.e., a lowering (lifting) of (un-)occupied states. This reduces the electronic contribution to the total energy and thus stabilizes the new phase. The opening of band gaps breaks the discrete translational symmetry of the system, which manifests itself in a periodic

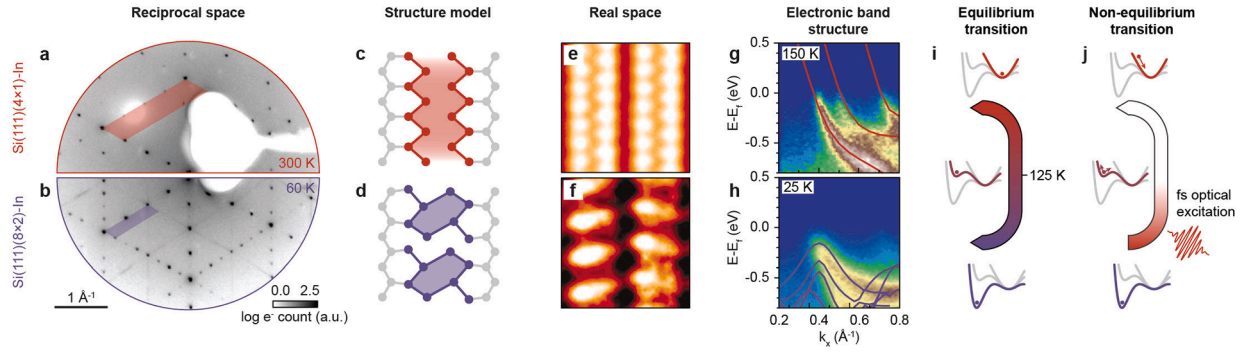

Fig. 2. Overview of the first-order transition between the metallic (4×1) (top) and insulating (8×2) (bottom) phase in atomic indium wires on Si (111). a, Low-energy-electron diffraction (LEED) pattern of the (4×1)-reconstructed surface, recorded with 130 eV electron pulses recorded at room temperature (T = 300 K) in our ULEED setup. b, LEED pattern of the (8×2)-reconstructed surface recorded at T = 60 K. The doubling of the unit cell both perpendicular and parallel to the indium wires leads to additional diffraction spots (8×) and streaks (×2). c,d, structure models of the (4×1) and (8×2) phase, featuring characteristic double chains or hexagons, respectively. Note that only a quarter of the (8×2) unit cell is shown in d. e,f, Real space topographies of indium wires recorded above (e) and below (f) T_c = 125 K. Adapted with permission from Ref. [115]. © 2004 by the American Physical Society. g,h, ARPES spectra recorded above (g) and below (h) T_c. Electronic bands have been calculated using density functional theory and are depicted in red and violet. Adapted from Ref. [63] with permission from AAAS. i,j, Schematics of the equilibrium and optically-excited nonequilibrium transition. (For interpretation of the references to color in this figure legend, the reader is referred to the web version of this article.)

modulation of the charge density $\rho(r)$ at a wavelength $\lambda_0 = \pi/k_F = 2a$ and with long-range order. Herein, the coupling of electrons and holes across the Brillouin zone is enabled by phonons with wave vector $q = 2k_F$ connecting opposite sections of the Fermi surface. This process is commonly referred to as Fermi surface nesting. At the same time, the phonons soften in frequency because of the strong electron–phonon correlations. As the phonon frequency $\omega_q \rightarrow 0$, the mode becomes macroscopically occupied, and a static periodic lattice distortion (PLD) with periodicity λ_0 is formed. However, this is at the expense of an increase in Coulomb repulsion between the ionic cores. Hence, the CDW transition is governed by the delicate balance between electronic and elastic energy [10,15].

Prominent materials exhibiting such a mechanism are organic linear chain compounds [22] or transition-metal bronzes [17,18]. In this review, we focus on the model system of quasi-one-dimensional self-assembled atomic indium wires on the (111) surface of silicon [55,56]. Fig. 2 provides an overview of the In/Si(111) surface system. Most importantly, approaching the critical temperature T_c, a Peierls-like structural phase transition transforms the surface between a metallic high-symmetry (Fig. 2a,c,e,g) and an insulating broken-symmetry phase (Fig. 2b,d,f,h) [55,57]. The stark structural and electronic changes within the atomic wires leave their signatures in diffraction [58,59], scanning tunneling microscopy (STM) [55,60,61] or angle-resolved photoemission spectroscopy (ARPES) [57,62], respectively (see Fig. 2a-h). Whereas the temperature-driven transition (Fig. 2i) is interesting in itself, e.g., because of its first-order nature that is hard to reconcile with a simple Peierls picture, the observation of nonequilibrium electronic [63–66] and structural [43,51,52,67,68] dynamics following ultrafast optical excitation (Fig. 2j) have enabled a number of fascinating conceptual insights, which we will discuss in the following.

2.2. The metallic (4×1) phase

As a substrate for the growth of the atomic indium wires, the (7×7)-reconstructed (111) surface of silicon is used. Single-crystalline silicon (Si) crystallizes in the diamond cubic crystal structure with a lattice constant a = 5.43 Å and an indirect electronic band gap of $E_{gap} = 1.1685$ eV at 60 K [69]. Freshly cleaved Si crystals typically exhibit a (2×1) surface reconstruction and need to be heated to temperatures $T > 850$ °C to overcome the energy barrier towards the (7×7) structure by means of thermal fluctuations.

The Si(111)(7×7) surface exhibits a variety of surface reconstructions caused by chemisorption of metal atoms, e.g., aluminum (Al) [70], lead (Pb) [71], gold (Au) [72,73], or indium (In) [70]. Herein, the making of chemical bonds between atoms of the topmost substrate layers and the metallic adatoms leads to strongly altered electronic [74–76], structural [56,70], or magnetic [46,77] properties compared with the corresponding pristine surfaces. Of particular interest is the self-assembly of quasi-one-dimensional metallic nanowires on different crystal faces of silicon, prominent examples being Pb on Si(557) [74], Ag on Si(557) [78], Sn on Si (557) [79], or Au on Si(553) [46,77]. Here, we focus on the most extensively studied of these atomic wire systems, namely, indium on

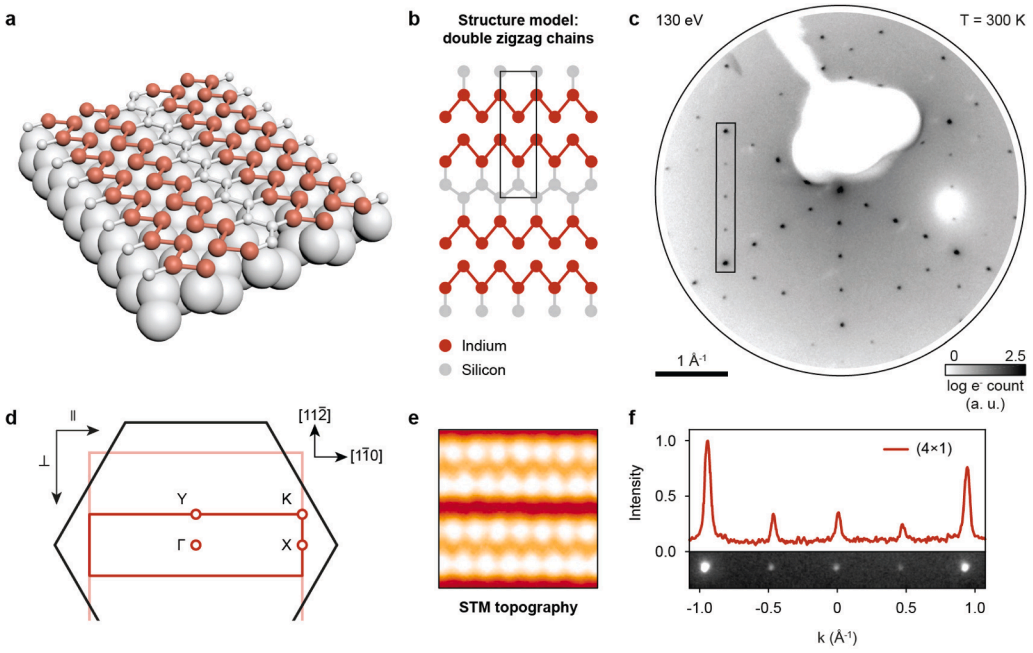

Fig. 3. Atomic structure of the (4×1) phase of indium on Si(111). a, Three-dimensional model of the In-induced (4×1) surface reconstruction. The In atoms arrange in pairs of parallel zigzag chains separated by single rows of Si atoms. Red, indium; gray, silicon. b, Structure model of the (4×1) phase. Black rectangle, unit cell. c, LEED pattern of the (4×1) structure recorded at room temperature with 130 eV electron pulses. Taken from Ref. [51]. d, Surface Brillouin zone (SBZ) of the (4×1) phase. Arrows on the left indicate orientation relative to the atomic chains. Hexagonal SBZ of the Si substrate shown in black. e, STM topography recorded at $U_{bias} = -0.15$ V and I = 20 pA; T = 135 K Adapted with permission from Ref. [115]. © 2004 by the American Physical Society. f, Selected regions and line-out from the LEED pattern (see black rectangle in c). Taken from Ref. [51]. (For interpretation of the references to color in this figure legend, the reader is referred to the web version of this article.)

Si(111). Morrison and Lander were the first to systematically investigate indium-induced reconstructions of the Si(111) surface using LEED [70], followed by Kawaji *et al.* [80] and Baba *et al.* [81], who completed and refined the phase diagram (see also Fig. 6a) by performing reflection high-energy electron diffraction (RHEED) measurements during growth of the indium layer at variable temperature. These initial studies of the surface yielded a cascade of surface reconstructions with increasing indium coverage and at substrate temperatures between 400 °C and 550 °C: a $(\sqrt{3}\times\sqrt{3})$R30° structure for coverages $c < 0.5$ ML, a $(\sqrt{31}\times\sqrt{31})$R9° structure for 0.4 ML $< c <$ 0.7 ML, a (4×1) structure for 0.5 ML $< c <$ 1 ML, and a $(\sqrt{7}\times\sqrt{3})$R9° structure for $c > 0.8$ ML (Fig. 6a). However, the Si(111)(4×1)-In surface has received special attention due to its microscopic structure, i.e., the formation of atomic quasi-one-dimensional metallic wires.

As mentioned above, the Si(111)(4×1)-In surface represents a model system for a various relevant issues in solid-state physics, among others, electronic and thermal transport in low-dimensional systems [82–84], phase transitions [55,59,85,86], as well as fluctuations [60,87], and the role of microscopic heterogeneity [48,60,61,88,89]. To this end, the (4×1) phase has been examined by a large number of different experimental methods, including LEED [59,70,90], I(V)-LEED [91], RHEED [67,83,92], reflective high-energy positron diffraction (RHEPD) [93], X-ray diffraction (XRD) [94], angle-resolved photoemission spectroscopy (ARPES) [57,62–66,75], Core-level PES [95], Auger-electron spectroscopy (AES) [92], electron energy loss spectroscopy (EELS) [96], reflectance anisotropy spectroscopy (RAS) [97–100], Raman spectroscopy [99,101,102], electrical transport measurements [83,84], STM [48,88,103–106], density functional theory (DFT) [97,107,108], and other theoretical approaches [86]. The system is a prime example of how the continuous development and advancement of novel methodologies in theory and experiment can contribute to a better understanding of processes in complex materials. In a sense, the system has always served as a benchmark for new techniques in the field of surface science since its discovery more than 50 years ago. With respect to the study of its nonequilibrium dynamics by cutting edge time-resolved techniques such as time-resolved ARPES (trARPES) [63–66] or ultrafast electron diffraction (UED) [43,51,52,67,68,109], this remains true today.

The quasi-one-dimensional structure of the (4×1) phase was recognized early by Cornelison *et al.* [110], Nakamura *et al.* [92], Saranin *et al.* [111,112], Pedreschi *et al.* [97] and Bunk *et al.* [94]. The structure model, widely accepted today, features double "zigzag" chains of indium atoms running along the [110], [011], and [101] directions of the Si(111) substrate. Indium double chains, in turn, are separated by single zigzag rows of silicon atoms (see Fig. 3b). Lower-lying layers of the substrate, on the other hand, remain largely unreconstructed [82], but may act as a charge reservoir [86,89,113,114]. Containing four indium and two silicon atoms, the (4×1) unit cell exhibits a two-fold rotation, a mirror as well as a glide plane, thus belonging to the "pmg" 2D space group [101] (see also Fig. 3b and d). The zigzag structure model agrees well with real-space topographies recorded by STM [55,103,115] (Fig. 3e) and the results of DFT calculations [116].

In LEED, the formation of the Si(111)(4×1)-In structure is accompanied by characteristic modifications of the initial diffraction pattern of the pristine Si(111) surface. Fig. 3c shows a LEED image of the (4×1)-reconstructed surface recorded with 130-eV electron pulses at $T = 298$ K in our ULEED setup. The quadrupling of the unit cell perpendicular to the chain direction leads to three additional spots between the Bragg spots of the Si substrate along [112], [121], and [211] directions. The existence of a three-fold instead of a two-fold rotation symmetry in the diffraction pattern stems from the use of precision-oriented Si(111) substrates with a tolerance of the cut angle of less than 0.1°. Such silicon wafers allow for the growth of indium chains along each of the three crystallographic directions connected by mutual rotations of 120°. As the electron spot diameter on the sample surface is significantly larger than the average size of the orientational domains, the LEED pattern represents an average over the three possible domain states. In this context, Stevens *et al.* [104] and Pedreschi *et al.* [97] investigated the growth of the (4×1) phase on vicinal surfaces, misaligned by up to 4° along, e.g., the [112] direction. Here, the surface exhibits a high density of parallel-running atomic terraces that facilitate the growth of single-domain indium nanowires along the [110] direction.

Although this review is mainly concerned with the structural dynamics in the In/Si(111) system, due to the strong coupling of electronic and structural degrees of freedom, many static and dynamic aspects can only be understood if the peculiarities of the electronic band structure are equally considered. For this reason, we provide a brief overview of the electronic structure of the (4×1)-reconstructed surface, whose highly anisotropic electronic band structure reflects the quasi-one-dimensional character of the atomic indium wires. ARPES has proven an ideal experimental tool to study the electronic properties of the system in and out of equilibrium. Summarizing previous results, the band structure of the (4×1) phase hosts three metallic bands m_1, m_2 and m_3 with nearly free-electron-like dispersion along the chain direction (Γ-X or $k_\parallel$, see Fig. 2e) and little to almost no dispersion perpendicular to the chains [57,62,75,117] (Γ-Y or $k_\perp$). In this respect, the system can be described by a multiband Peierls model. The anisotropy of the band structure also has a measurable impact on the macroscopic surface conductance, as evidenced by transport measurements along and perpendicular to the chain direction [84]. Concerning the individual metallic bands, m_1 exhibits a filling factor of $\eta = 0.11$ and crosses the Fermi energy E_F at $k_\parallel = 0.75$ Å^{-1}, forming a small electron pocket around the K point [57]. The m_2 band ($\eta = 0.38$) crosses E_F at $k_\parallel = 0.54$ Å^{-1} and shows a somewhat weaker dispersion in Γ-Y direction. Remarkably, the m_3 band is exactly half-filled ($\eta = 0.50$) and crosses E_F at $k_\parallel = k_F = 0.41$ Å^{-1}. In addition, this band exhibits no significant dispersion along Γ-Y, and therefore fulfills the necessary condition for Fermi-surface nesting, i.e., half-filled bands with large parallel sections of the Fermi surface.

2.3. The insulating (8×2) phase

The close resemblance of the electronic band structure of the (4×1)-reconstructed surface to the metallic state of a one-dimensional Peierls model already suggests that below a certain critical temperature T_c, the structure is unstable to a dimerization and, thus, a spontaneous transition into a new, symmetry-broken ground state. Therefore, it may not be surprising that in 1999, Yeom *et al.* [55] reported a reversible metal–insulator phase transition of the Si(111)(4×1)-In surface to a (4×"2"), or later, (8×2) phase for

temperatures below T_c = 125 K. Despite the clear signature of the phase transition in a number of experiments with different observables, it took more than ten years to develop both a robust structure model for the low-temperature phase as well as a comprehensive understanding of the mechanism and driving forces for the transition. Because of the intertwined nature of electronic and lattice subsystems, the problem could only be solved by a combination of several experimental techniques with complementary sensitivities and a close collaboration between theory and experiment.

The result of this process, i.e., the widely-accepted structure model for the low-temperature Si(111)(8×2)-In phase, is summarized in Fig. 4a and b. Below T_c, the indium atoms within the wires rearrange in a hexagonal bonding motif. While the formation of hexagons leads to a doubling of the unit cell along the wires, strong correlations between the internal structures of neighboring wires, i.e., an anti-phase arrangement of hexagons, cause the unit cell to double in the perpendicular direction. The transition to this new structural configuration involves two characteristic types of changes. First, a Peierls-like dimerization of the outer indium rows, corresponding to the weakening/strengthening of In-In bonds in alternating order. Second, a mutual shearing of neighboring zigzag chains, reflected in the modification of bonds between the two inner indium rows. DFT calculations predict the hexagon model to be semiconducting with no bands crossing the Fermi level [85,118,119], as is confirmed by ARPES measurements on the Si(111)(8×2)-In surface (see also Fig. 2h). Moreover, the hexagon model is consistent with the characteristic signature of the low-temperature phase in STM topography measurements (see Fig. 4e).

The LEED pattern of the Si(111)(8×2)-In phase shows seven additional spots between the Bragg peaks, reflecting the strong wire-to-wire correlation in the direction perpendicular to the wires in agreement with X-ray diffraction [58] and RHEED [43,59,67,83] (see Fig. 4c). Moreover, the two-fold streaks, first noted by Yeom *et al.* [55], are clearly visible. These streaks result from correlations of different strengths between neighboring (4×2) wires along or perpendicular to the wire direction [58]. To understand this, we first note that the (4×1) and (8×2) reconstructions are both commensurate with respect to the silicon substrate. Hence, for the (8×2) structure, there exist two possible mutual arrangements of hexagons in neighboring wires, namely 'in-phase' and 'out-of-phase'. Within a single (4×2) wire, the correlation of the (×2) surface elementary cells along the chains is strong, causing sharp (×2) features along the corresponding direction in LEED (i.e., horizontal in Fig. 4c). For adjacent (4×2) wires, however, the two possible relative phases between the (×2) elementary cells significantly reduce the correlation perpendicular to the wires, which in turn leads to the smearing of the (8×) LEED spots in the corresponding direction (i.e., vertical in Fig. 4c) and thus to the formation of streaks. In contrast, the sharp (8×) first-order spots indicate very strong correlations perpendicular to the wire direction, that is, a well-developed (8×) superstructure [58]. Containing 16 indium and eight silicon atoms, the (8×2) unit cell exhibits only a glide plane, and is therefore classified as a "pg" 2D space group [101] (see also Fig. 4b,d).

As mentioned above, a comprehensive model of the In/Si(111) system has to describe not only the atomic structure of the low-

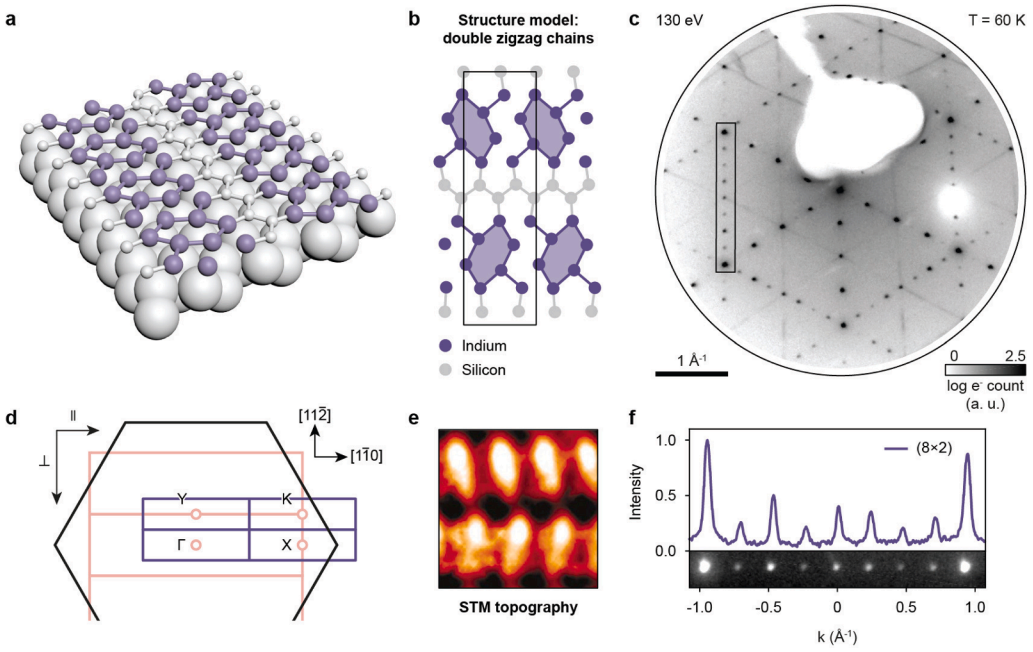

Fig. 4. Atomic structure of the (8×2) phase of indium on Si(111). a, Three-dimensional model of the In-induced (8×2) surface reconstruction. The In atoms arrange in hexagons separated by single rows of Si atoms. Violet, indium; gray, silicon. b, Structure model of the (8×2) phase. Black rectangle, unit cell. c, LEED pattern of the (8×2) structure recorded at T = 60 K with 130 eV electron pulses. Taken from Ref. [51]. d, Surface Brillouin zone (SBZ) of the (8×2) phase (violet) and the (4×1) phase (light red). Arrows on the left indicate orientation relative to the atomic chains. Hexagonal SBZ of the Si substrate shown in black. e, STM topography recorded at U_{bias} = -0.15 V and I = 20 pA; T = 78 K. Adapted with permission from Ref. [115]. © 2004 by the American Physical Society. f, Selected regions and line-out from the LEED pattern in c (see black rectangle). Taken from Ref. [51]. (For interpretation of the references to color in this figure legend, the reader is referred to the web version of this article.)

temperature phase, but also its electronic structure and the phase transition. Therefore, the following paragraph will elucidate the electronic band structure of the (8×2) phase. Mirroring the structural modifications, the electronic band structure of the Si(111)(4×1)-In surface also changes drastically across the phase transition at T_c. As a main observation, the system undergoes a metal–insulator transition, as the three relevant metallic bands of the (4×1) phase no longer cross the Fermi level at any point of the Brillouin zone [57,62]. This may seem surprising, given that only the m_3 band meets the conditions for Fermi-surface nesting. However, a temperature-dependent upshift of the m_1 band (filling factor $\eta = 0.12$) above E_F and the resulting charge transfer to m_2 ($\eta = 0.38$) leaves this band half-filled ($\eta^* = 0.38 + 0.12 = 0.50$) with $k(E_F) \approx k_F$ [57]. Just like the atomic lattice, the low-temperature electronic band structure exhibits a doubled periodicity both along and perpendicular to the chain direction (Γ-X, or Γ-Y direction, respectively), as evidenced by Fermi-contour measurements [57,62]. It further shows two characteristic band gaps around the $\Gamma_{(8\times2)}$ point ($\Delta E_{g,\Gamma} \approx$ 1.0 eV), and the $X_{(8\times2)}$ point ($\Delta E_{g,X} \approx 0.3$ eV) both of which are smaller than the band gap of the Si substrate ($\Delta E_{g,Si}(60\ K) = 1.1685$ eV). While the opening of the band gap at k_F might be interpreted as a multi-band Peierls transition, the necessary interband and intraband charge transfer cannot be explained in this picture and thus points to an additional, supporting mechanism. Hence, the question remains how the interaction of structural and electronic degrees of freedom enables both the charge transfer around Γ and the gap opening around X, i.e., the metal–insulator transition.

2.4. Decisive structural modes

From the above considerations it is apparent that the (8×2)→(4×1) phase transition is governed by specific structural distortions of the initial (8×2) structure as well as modifications of the electronic band structure. Considering the eminent role of electron–phonon coupling in Peierls systems, it can be assumed that these characteristic changes occur in a cooperative manner, i.e., by means of electronic and lattice subsystems mutually influencing each other in the transition. For In/Si(111), this aspect has been studied in theory [85,86,119–126] and experiment [48,57,63]. Here, we aim to understand the transition from a lattice perspective first and begin by analyzing distortions transforming the high-symmetry (4×1) into the low-symmetry (8×2) structure. We will then continue by a more detailed review of lattice modes relevant for the (non–)equilibrium (8×2)→(4×1) transition.

Despite the complex atomic displacement pattern connecting (4×1) and (8×2) phases, it has been shown that the transformation between high- and low-symmetry structures is realized by a small set of phonons of the initial phase [85,119,124,125]. Identification of these ‘key’ or ‘decisive’ phonons necessitates detailed insights into the surface vibrational modes of the indium monolayer. Combining high-resolution Raman spectroscopy with frozen phonon calculations in DFT, Fleischer *et al.* [102] and Speiser *et al.* [101] explored the vibrational properties of the (4×1) and (8×2) surfaces, identifying a large number of modes with wave numbers between 10–90 cm^{-1} ($\hbar\omega_{ph} \approx$ 1–11 meV), which is the relevant energy range for phonon modes related to the displacement of indium atoms. Almost all of these modes are substantially occupied at T_c and may therefore contribute to the phase transition, since their energy is smaller than $k_B T_c = 10.7$ meV.

Density functional theory has been harnessed to identify modes that are associated with the transition. Specifically, Wippermann et al. [85] demonstrated that by breaking down the hexagonal structure into phonon eigenvectors of the (4×1) phase, a combination of

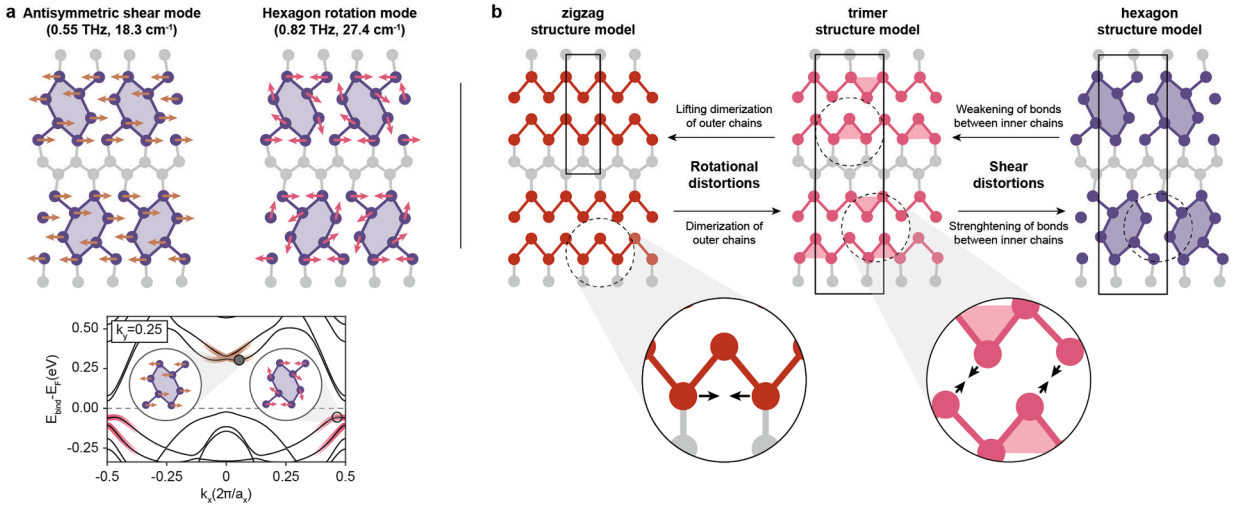

Fig. 5. Shear and rotation modes of the (8×2) structure and their role in the (8×2)→(4×1) transition. a, (Top) Golden and pink arrows indicate the normalized eigenvectors of the antisymmetric shear and hexagon rotation phonon modes, respectively. Grey, silicon atoms; violet, indium atoms. (Bottom) Coupling of shear and rotation modes to states at the Γ ($k_x = 0/a_x = 0.0$ $Å^{-1}$) and X ($k_x = \pi/a_x \approx 0.4$ $Å^{-1}$) points in the electronic band structure of the (8×2) phase. Band structure taken from Ref. [52]. b, Role of shear and rotational distortions in the phase transition. Black arrows indicate the direction of atomic motion corresponding to shear or rotation distortions. Note that while rotation and shear modes comprise the motion of almost all atoms within the unit cell, only particular motions of the In lattice have been highlighted. (For interpretation of the references to color in this figure legend, the reader is referred to the web version of this article.)

a soft shear mode and two degenerate rotation modes transforms the (4×1) structure into the (8×2) structure with an accuracy of 0.01 Å average displacement per atom. This raises the question of how these modes are connected to changes in the electronic structure of the (4×1) phase as the temperature approaches T_c. The relationship between shear and rotation modes on the one hand, and the electronic band structure on the other hand, was investigated both theoretically and experimentally in the case of the (4×1)→(8×2) transition. Summarizing previous works, a comparison of the high- and low-temperature band structures reveals significant changes, particularly near the $\Gamma_{(8\times2)}$ ($X_{(4\times1)}$) and the $X_{(8\times2)}$ points. According to DFT, shear and rotation modes are intricately linked to electronic states in these regions of the Brillouin zone: a shear distortion of the indium chains elevates the m_1 band around $\Gamma_{(8\times2)}$ ($X_{(4\times1)}$) above the Fermi level and initiates the charge transfer to m_2 [67]. At the same time, rotational motion causes the dimerization of the outer chain, resulting in the opening of a gap at $X_{(8\times2)}$ (Fig. 5a, right).

So far, we have discussed the transition from the (4×1) to the (8×2) phase, which occurs when the surface is cooled below T_c. In the next step, we consider the opposite scenario, namely the (8×2)→(4×1) transition that occurs when the low-temperature phase is heated or photo-excited. Similar to the (4×1)→(8×2) transition, specific vibrational modes play a crucial role in realizing this structural transition. However, the high- and low-temperature phases have different symmetries and exhibit distinct sets of structural modes, which have been identified through temperature-dependent Raman measurements [86,101,102]. The notable changes in the Raman spectra between the (4×1) and (8×2) phases are a result of the folding of edge modes of the (4×1) surface Brillouin zone (SBZ) to the Γ point of the (8×2) SBZ, alongside changes in phonon frequencies due to modifications of the atomic structure. Additionally, the doubling of the surface elementary cell along and perpendicular to the indium chains leads to an increase in the number of modes. Consequently, representing the ideal (4×1) structure using the eigenvectors of the (8×2) vibrational modes reveals two new key modes for the (8×2)→(4×1) transition: an antisymmetric shear mode at $f = 0.55$ THz (18.3 cm^{-1}, left side in Fig. 5a) and a hexagon rotation mode at $f = 0.82$ THz (27.4 cm^{-1}, right side in Fig. 5a) [67,101].

In the (8×2)→(4×1) transition, a displacement of the antisymmetric shear mode associated with electronic states around the $\Gamma_{(8\times2)}$ point shifts the m_1 band below E_F (golden bands in Fig. 5a, bottom) [63,64]. This corresponds to a weakening of bonds between the inner indium rows. On the other hand, a rotational displacement closes the gap (m_2, m_3) at $X_{(8\times2)}$, and thus lifts the dimerization of the outer indium rows (pink bands in Fig. 5a, bottom). An overview of the role of shear and rotation distortions in the (4×1)→(8×2) and (8×2)→(4×1) transitions is given in Fig. 5b.

In addition to the microscopic mechanisms underlying the phase transition and the coupling of electron and phonons therein, the question of whether the transition is of first or second order was discussed intensively [59]. At the atomic level, STM provided unambiguous evidence for the coexistence of (4×1) and (8×2) phases well below T_c [48,60,61], pointing to the existence of a supercooled high-symmetry phase, and thus, to a first-order transition. Moreover, Raman studies [101,102] found distinct, yet similar sets of modes for both phases, indicative of a first-order scenario. A macroscopic signature of a first-order transition was found by Klasing *et al.* [59], who observed a robust hysteresis of 8.6 K for heating/cooling rates between 0.05 and 0.35 K s^{-1} in temperature-dependent LEED measurements. Another argument is provided by the band structure changes described above. Specifically, in the (4×1)→(8×2) transition, the charge transfer between m_1 and $m_{2,3}$ bands and the resulting energy gain due to the formation of the Peierls gap at $X_{(8\times2)}$ necessitates the uplifting of states around the Γ-point at the cost of electronic energy. This energy can be associated with the characteristic barrier that has to be overcome in a first-order phase transition. The energy barrier separating the (8×2) and (4×1) phases plays an integral role in the coherent control of the transition, which is discussed further below.

3. Experimental aspects

3.1. Sample preparation

An experimental aspect that is perhaps underrepresented, or underappreciated, in the literature on the phase transition in atomic wires on silicon is the challenging preparation of the Si(111)(8×2)-In surface. For this reason, we discuss the essential steps in the preparation of samples for ULEED and OPP experiments in more detail. A fundamental issue in surface science is posed by adsorption of atoms or molecules from the residual gas, which can significantly alter the physical and chemical properties of a surface. In this respect, atomic indium wires on the Si(111) surface represent a particularly striking example. Specifically, as described in Refs. [61,83,89,114,127], different types of adsorbates or defects on the Si(111)(8×2)-In surface lead to distinct modifications of the surface, e.g., shifts of the critical temperature T_c of the transition [93], changes in the hysteresis width [90,127], alteration of the local barrier heights for the (8×2)↔(4×1) transition [48,51], or pinning of the high temperature (4×1) phase below T_c [93,127]. We note that these effects, which are typically treated as perturbation effects in spatially averaging studies, can be of great interest on an atomic scale, and they may drastically affect the lifetime of the laser-induced metastable state [43]. Moreover, as shown by scanning tunneling microscopy and spectroscopy [48], individual adatoms can significantly affect the spatial extensions of metal–insulator junctions.

In ULEED, the low-temperature phase (8×2) and the optically excited transition into the metastable state (4×1) can be investigated over a period of several hours to a maximum of one day in a single experimental run, depending on the condition of the substrate and the background pressure. The main limiting factor is given by the adsorption of adatoms and molecules from the residual gas and the associated local pinning of the high-temperature structure below T_c. This effect significantly reduces the leverage of optical excitation in pump–probe measurements of the (8×2)→(4×1) transition and studies on the coherent control of the transition efficiency. A particularly strong contamination of the surface is observed after a temporary heating of the specimen, e.g., during thermal cycling between high and low temperature phases. This is due to the desorption of residual gas atoms from the cryo-manipulator during heating and the subsequent adsorption on the sample at lower temperatures. Therefore, to ensure the comparability of data measured in different runs of the experiment, sample preparation must always take place under identical conditions, i.e., in an ultra-high vacuum

environment at a typical base pressure $p < 2 \cdot 10^{-10}$ mbar. In addition, the composition of the residual gas in the UHV chamber is of particular importance. Even for identical preparation parameters, In/Si(111) surfaces prepared in two different setups are expected to differ in terms of their local atomic structure. Generally, when comparing, e.g., the observed thresholds and leverages of optical excitation for two distinct measurements, only data recorded on samples of approximately the same age should be considered.

As for the preparation routine preceding ULEED experiments, Si(111)(8×2)-In surfaces were obtained by flash-annealing Si(111) wafers (3×11 mm; phosphorous doped; resistivity $R = 0.6$–$2\ \Omega$ cm; tolerance of the cut angle $< \pm 0.1°$) at $T_{max} > 1250$ °C via direct-current heating (DCH). We note that the doping of the silicon wafers can have a significant impact, e.g., on the transition temperature. Furthermore, using Si(111) substrates with a miscut of 2° along the [1 1–2] direction results in the presence of atomic terrasses with a mean width of (298 ± 8) nm, and thus facilitates the growth of large arrays of indium chains with a preferential orientation along the terrasses [68]. For such samples, ULEED patterns clearly show a dominating contribution of indium chains along the corresponding direction in momentum space. To be able to control the temperature T during the preparation process, a pyrometer (Optris CTvideo 1MH) was used to measure the surface temperature of the wafer as a function of the current I. Fig. 6b shows the result of such a calibration measurement, which is typically performed on a fresh wafer. Based on this calibration, a clean Si(111)(7×7) reconstruction was prepared by pre-annealing the surface at $T^{Si}_{anneal} = 900$ °C, flashing for 5 s at temperatures $T_{max} > 1250$ °C, and subsequent post-annealing at 900 °C (typically three cycles, see Fig. 6c). The maximum pressure during flashing was kept below $p_{max} = 2 \cdot 10^{-9}$ mbar. Depending on the vacuum setup, this can only be achieved by outgassing samples at elevated temperatures $T > T^{Si}_{anneal}$ beforehand, or after multiple flash-anneal cycles, while the manipulator is cooled to prevent heating and outgassing of the sample environment. Silicon substrates can usally be used several times to prepare the Si(111)(4×1) surface. However, there are aging effects. In the case of insufficient background pressure levels or flash temperatures during preparation, the formation of SiC and SiO_2 results in extremely rough surfaces with a hazy optical appearance may form over time.

The indium nanowire arrays were grown by evaporating 1.2 monolayers (ML) of indium at a rate of about $8 \cdot 10^{-3}$ ML/s onto the Si (111)(7×7) surface reconstruction at room temperature (see also the phase diagram in Fig. 6a). The Si(111)(4×1)-In surface is then prepared by subsequent annealing at $T^{In}_{anneal} = 500$ °C for 300 s using DCH (see Fig. 3c). It should be noted that the Si(111)(4×1)-In surface can also be prepared in a single step, i.e., by deposition of indium while the sample is held at the annealing temperature [70,109]. After inspection of the freshly prepared surface in our ULEED setup, the samples were immediately cooled down to a base temperature of $T < 60$ K using an integrated continuous-flow helium cryostat. The phase transition between the high-temperature (4×1) and the low-temperature (8×2) phases was consistently observed at 125 K, which indicates a relatively low initial density of adsorbates on the pristine Si(111)(4×1)-In surface.

3.2. *Ultrafast low-energy electron diffraction (ULEED)*

Low-energy electron diffraction (LEED), with its ability to investigate the formation of long-range structural order and determine the atomic structure of crystalline surfaces with sub-Ångstrom resolution, has become an indispensable tool of surface science [128,129]. The ultimate surface sensitivity of LEED stems from the extremely short inelastic mean free path of electrons with kinetic energies between 20 and a few hundred electron volts (see Fig. 7b). In this energy range, only those electrons scattered within the topmost atomic layers of a solid exhibit a non-vanishing probability for purely elastic scattering and can thus interfere coherently to form sharp features, i.e., diffraction spots or streaks, in the LEED pattern.

Generally, LEED represents an ideal complement to bulk-sensitive structural probes based on the interaction of electrons or light with matter, such as transmission electron microscopy (TEM) [130] or X-ray diffraction (XRD). Many of these techniques were successfully combined with stroboscopic illumination schemes to facilitate the observation of ultrafast structural dynamics in the bulk by means of pump–probe experiments [33,131,132]. However, despite major achievements in the development of time-resolved reflection high-energy electron diffraction (trRHEED) [43,67,68,109] for the investigation of surface structural dynamics, an

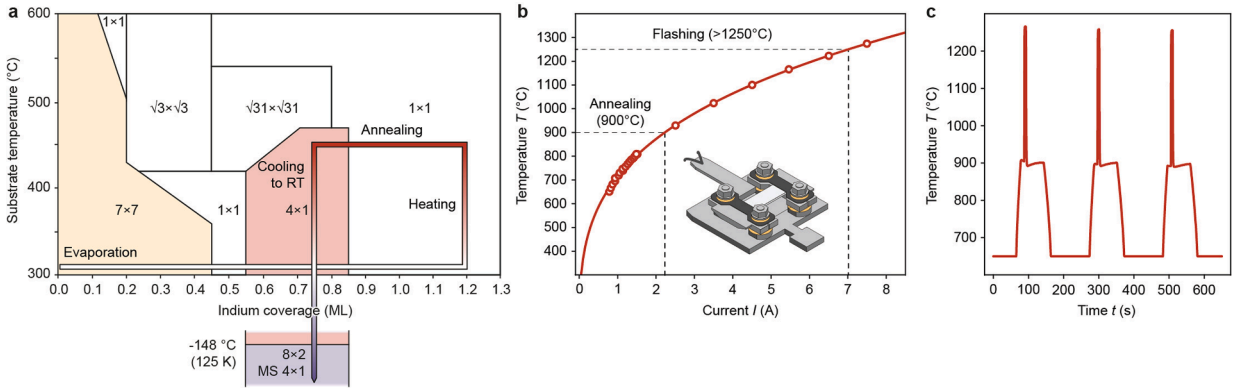

Fig. 6. Preparation of Si(111)(4×1)-In and Si(111)(8×2)-In surfaces. a, Phase diagram of indium-induced reconstructions of the Si(111) surface as a function of indium coverage and substrate temperature. Adapted from Ref. [80]. b, Substrate temperature recorded by a pyrometer as a function of the current applied in DCH. Inset: Typical sample holder used in experiments. c, Flash-anneal cycles used to prepare a clean Si(111)(7×7) surface.

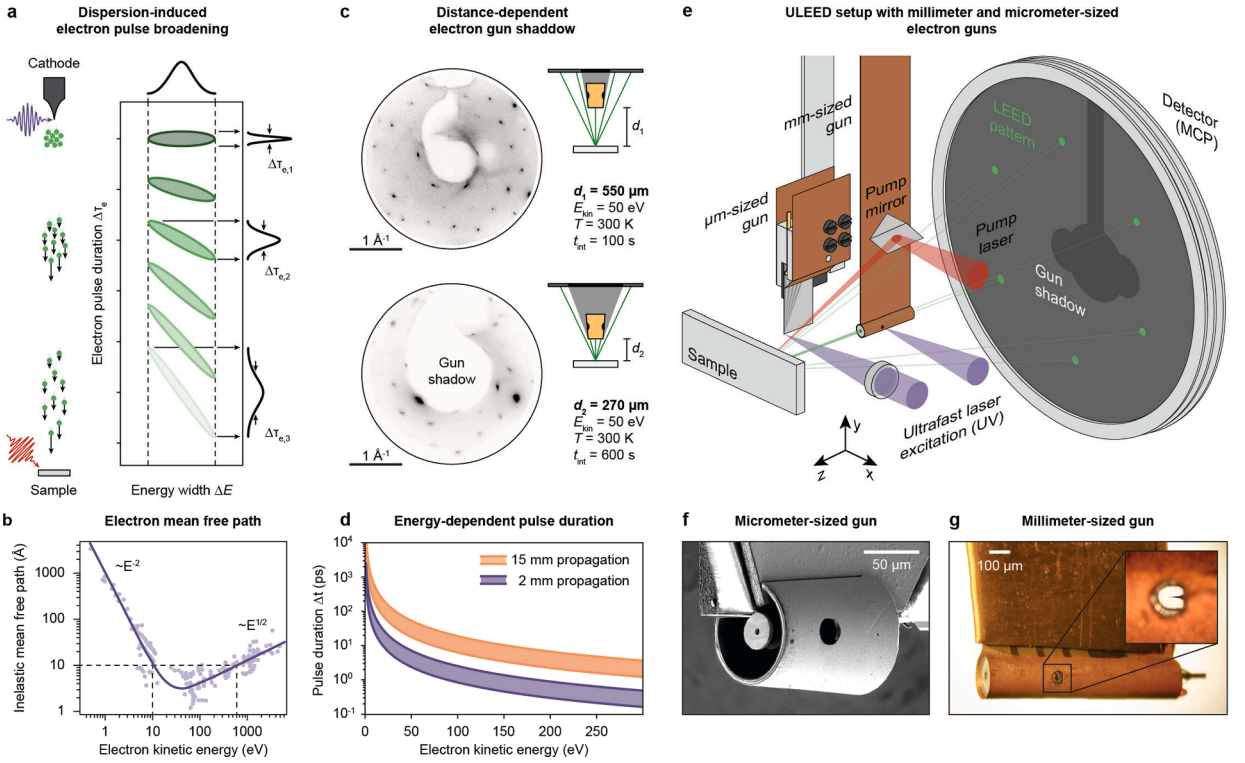

Fig. 7. Principles and technical realization of ultrafast low-energy electron diffraction. a, Schematic of the dispersion-induced electron pulse broadening during propagation between photocathode and sample surface. b, Energy-dependent electron mean free path in solids with a minimum between 20 eV and 150 eV. c, Electron gun shadow on the micro-channel plate detector for two distances micrometer-sized gun and sample. d, Calculated electron pulse durations at the sample surface as a function of electron kinetic energy shown for two gun-sample distances. e, Experimental ULEED setup with millimeter- and micrometer-sized gun. f, Scanning electron micrograph of the micrometer-sized gun. g, Optical microscope image of the millimeter-sized gun.

ultrafast implementation of LEED (ULEED) remained highly desirable but elusive.

The main reason for this is the dispersion-induced broadening of electron pulses in space and time during the propagation between the electron source and the sample surface (see Fig. 7a) [133]. Typically, electron bunches for diffraction and imaging are generated by ultrashort light pulses triggering a photocathode. The photoemission process endows the electron pulses with a finite energy distribution which results in a propagation-induced shearing of the phase space density. A projection on the time axis (in the rest frame of the electron pulse) highlights the resulting temporal broadening that limits the temporal resolution of the experiment. This effect is particularly severe for low-energy electron pulses, as the pulse duration Δt increases as a function of the propagation time, which is significantly longer in a standard LEED setup compared with a TEM. Coulomb repulsion, on the other hand, being the limiting factor for many electron diffraction experiments [134], is minimized in ULEED by limiting the average number of electrons per pulse to $n \approx 1$. The most straightforward strategy to limit the effect of dispersion-induced broadening is to reduce the propagation distance between the electron source and the sample. Fig. 7d shows energy-dependent electron pulse durations calculated for two exemplary propagation distances (15 mm and 2 mm). For 100 eV electrons, the difference in temporal resolution amounts to one order of magnitude (20 ps or 2 ps, respectively). At the same time, since electrons are recorded in a back-scattering geometry, the finite size of the LEED gun and its shadow on the detector pose a significant challenge for the experimental implementation of ULEED (see Fig. 7c). More specifically, smaller working distances require miniaturized laser-triggered LEED guns to ensure a sufficiently large fraction of the detector area can be used to record the diffraction pattern.

Enabled by the development of two miniaturized, laser-triggered LEED gun designs [133,135] (Fig. 7f,g), we have realized ULEED in an optical-pump/electron-probe scheme with down to 1-ps temporal resolution for the investigation of structural dynamics at surfaces [51,52,135–138]. To this end, electron pulses are generated by illuminating a tungsten needle emitter with an apex radius of few tens of nanometers with femtosecond laser pulses (central wavelength 400 nm, pulse duration 45 fs, pulse energy < 20 nJ) at repetition rates of up to 100 kHz. The electron beam is subsequently accelerated and collimated by four metal electrodes functioning as a suppressor-extractor unit, and an electrostatic einzel lens to probe the momentary state of the sample surface. The millimeter-sized gun (Fig. 7g) is based on precision machined, cup-shaped electrodes, polyimide (Kapton) rings for insulation, and a flexible printed circuit board. It delivers electron pulses with a minimum duration of $\Delta t^{mm} = 16$ ps at a working distance of a few millimeters and a momentum resolution of $\sigma_k^{mm} = 0.030$ Å^{-1} corresponding to a transfer width of $w^{mm} = 21$ nm. The micrometer-sized gun, on the other hand, is fabricated by focused ion beam milling in combination with electron beam lithography [133] and allows for gun-sample

distances of the order of 100 μm. In this configuration, the gun provides a temporal resolution of $\Delta t^{\mu m} = 1$ ps and a momentum resolution of $\sigma_k^{\mu m} = 0.067$ Å^{-1} ($w^{\mu m} = 9$ nm).

For the optical excitation of the surface, ultrashort optical pulses from the output of the laser amplifier, a noncollinear optical parametric amplifier (NOPA), and/or a collinear OPA are guided onto a motorized delay stage for precise timing of the sample excitation relative to the electron probe pulse and are subsequently focused onto the sample. Optical pulse sequences are either created by combining the different outputs of the laser system via dichroic mirrors or in a Michelson interferometer inserted into the beam path. In a prototypical ULEED measurement, backscattered electrons from the surface are amplified and recorded by a combination of a chevron microchannel plate, a phosphor screen and a cooled sCMOS (scientific complementary metal–oxide–semiconductor) camera for selected pump–probe delays. Integration times are of the order of $t_{int} = 20$ s per frame in time-resolved experiments.

The capabilities of ULEED have so far been demonstrated in studies on the dynamics of polymer chains on graphene [136], nonequilibrium heat-transfer of physisorbed molecular layers [138], μm-scale surface reconstructions [139], as well as ultrafast dynamics in charge density waves [51,52,135,137]. In the present contribution, we focus on the structural dynamics in atomic indium wires on the (111) surface of silicon to demonstrate the advances in ULEED, enabling novel insights on nonequilibrium structural phase transitions and their all-optical control.

4. Ultrafast probing of the (8×2)→(4×1) transition

4.1. Time-domain signatures of the transition

The electronic and structural dynamics following single-pulse optical excitation of the Si(111)(8×2)-In surface in the near-infrared regime have been investigated in a series of trARPES [63–66] and trRHEED [43,46,67,109] experiments. From a band-structure perspective, ultrafast optical excitation of the atomic wire system transiently populates conduction band states across the entire Brillouin zone and creates localized photoholes at the X-point [63–65]. The resulting redistribution of charge density in real space (for details, see Fig. 10) subsequently initiates nuclear motion according to the displacement patterns of shear and rotation modes (see Fig. 5a). Strong and exclusive coupling of electronic excitations to these phonons enables the transition into the metastable (4×1) phase in the limit of directed or 'ballistic' atomic motion and without raising the overall lattice temperature above T_c [51,67,109]. This is in stark contrast to a number of other light-driven transitions in charge density wave materials that are driven by a transient excitation of multiple structural modes, many of which do not play an active role in the transition.

In this context, ULEED allows us to investigate the structural dynamics underlying the optically-induced (8×2)→(4×1) transition with unprecedented sensitivity. For this, the Si(111)(8×2)-In surface at $T = 60$ K is illuminated by femtosecond light pulses (photon energy $\hbar\omega = 1.20$ eV) at a repetition rate of $f_{rep} = 100$ kHz. The diffraction pattern is recorded as a function of the delay $\Delta t_{p\text{-}el}$ between optical excitation and the electron pulses ($E_{kin} = 80$–130 eV), probing the momentary surface structure. Fig. 8a presents LEED patterns recorded before ($\Delta t_{p\text{-}el} < -80$ ps) and after ($\Delta t_{p\text{-}el} > +75$ ps) time-zero ($\Delta t_{p\text{-}el} = 0$). The pump-induced changes in the diffraction pattern are apparent from the difference image in Fig. 8b, which is generated by subtracting images recorded before and after the arrival of the

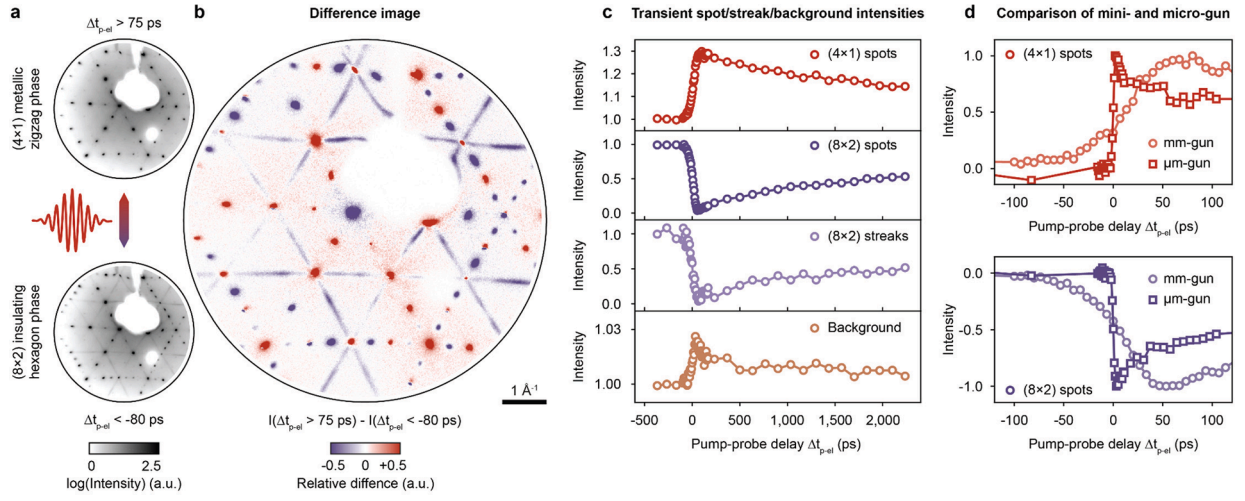

Fig. 8. Optically-induced nonequilibrium transition between (8×2) and (4×1) structures observed by ULEED. a, LEED images recorded before and after excitation by single femtosecond light pulses (incident fluence $F = 1.7$ mJ cm^{-2}). b, Difference image obtained by subtracting images in a. White area, electron gun shadow. c, Delay-dependent intensities of (top to bottom) (4×1) and (8×2) diffraction spots, (×2) diffraction streaks and the inelastic background signal. d, Comparison of delay-dependent intensities of (4×1) (top) and (8×2) (bottom) diffraction spots extracted from measurements with the millimeter-sized gun (light red/light violet circles) or the micrometer-sized gun (red/violet rectangles), respectively. The datasets have been normalized to minimum/maximum intensity to facilitate comparison. (For interpretation of the references to color in this figure legend, the reader is referred to the web version of this article.)

pump pulse at the surface. We identify three main features linked to the structural phase transition: (1) Fourfold spots which are present in both the (4×1) and the (8×2) LEED pattern show an increase in intensity due to changes in the structure factor [115]. (2) The eightfold spots and twofold streaks of the (8×2) structure are suppressed, as they are linked to hexagon/CDW formation and unit-cell doubling in the broken-symmetry state. More specifically, the transition into the high-symmetry (4×1) state and the melting of the CDW modify the structure factor, which is reflected in the diffraction pattern. (3) The diffuse background level increases due to the excitation of phonons of the indium monolayer and the subsequent transfer of energy to a manifold of low-lying structural modes of the substrate via phonon–phonon coupling, resulting in a diffuse intensity distribution in *k*-space.

Next, we analyze the temporal evolution of these different features as a function of the pump–probe delay. To this end, at each delay step, we sum up the background-corrected raw intensities in the diffraction pattern within areas of interest around (4×1) and (8×2) spots, (8×2) streaks, as well as regions dominated by the diffuse background signal (details on data analysis can be found in Ref. [51]). Exemplary traces of each feature, recorded in experiments with the millimeter-sized electron gun, are shown in Fig. 8c as a function of $\Delta t_{\text{p-el}}$. Within the temporal resolution of our experiments, we find a mirror-like enhancement/suppression of (4×1)/(8×2) spot intensities and a subsequent relaxation to their initial values on a few-nanosecond timescale. This behavior not only reflects the metastability of the photo-excited (4×1) state, but also the first-order character of the (4×1)↔(8×2) transition for which ground state recovery is expected to occur via nucleation and growth of (8×2) domains at a fixed velocity v_{rec} along the chain direction [43,68]. The relative changes to the (4×1) and (8×2) intensities observed in the nonequilibrium transition are in qualitative agreement with static LEED and SPA-LEED measurements [127].

Furthermore, ULEED experiments on the ultrafast phase transition employing the micrometer-sized gun allow for a tracking of transient changes in the diffraction pattern with an order-of-magnitude higher temporal resolution. Fig. 8d compares delay-dependent traces of (4×1) and (8×2) diffraction peak intensities recorded with the millimeter- (light red/violet circles) and the micrometer-sized gun (red/violet rectangles). In particular, the microgun data evidences the fast initial excitation of the metastable (4×1) state within the temporal resolution of the experiment (here ≈ 3 ps). At the same time, these measurements also reveal a fast partial recovery of the ground state to a more persistent level within the first 100 ps, which will be analyzed and discussed in detail further below. Before that, however, we review results on the structural dynamics occurring within the first few picoseconds after optical excitation.

4.2. Initial structural dynamics

To access the timescale of the initial dynamics of the (8×2)→(4×1) transition, we complement ULEED with optical pump–probe spectroscopy (OPP). More specifically, we perform transient reflectivity measurements at the Si(111)(8×2)-In surface (Fig. 9a). OPP is

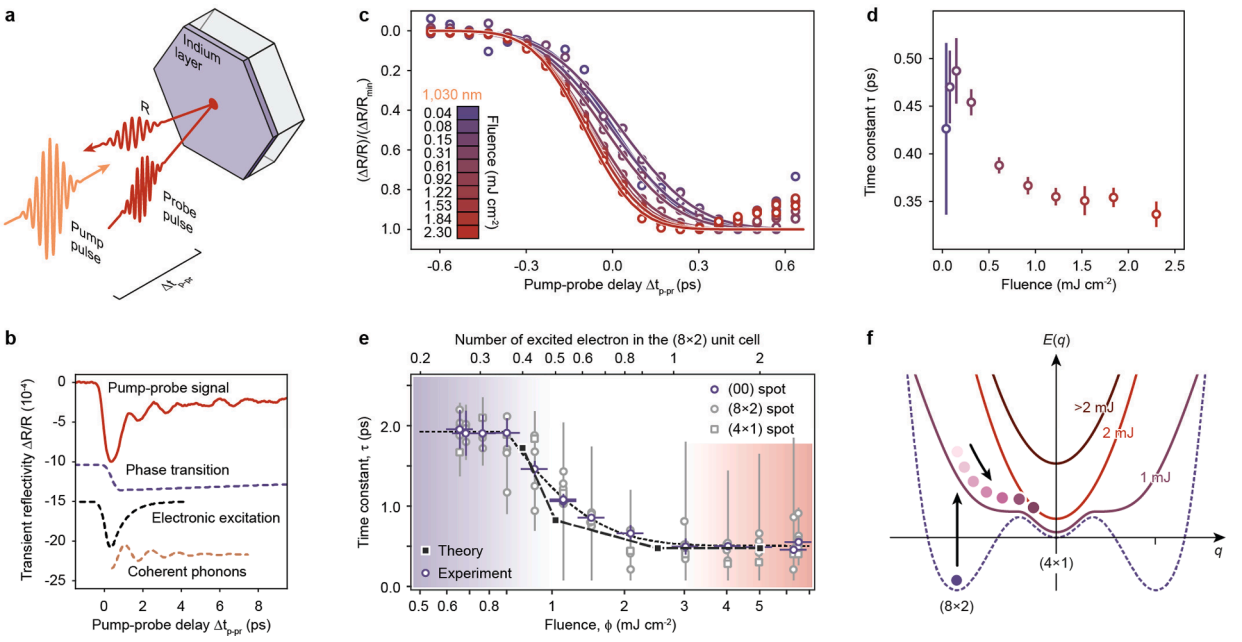

Fig. 9. Initial dynamics following single-pulse optical excitation. a, Schematic of transient reflectivity measurements. b, Exemplary scheme of an OPP trace, showing the typical signatures of different contributions to the transient reflectivity of a surface. c, Normalized transient reflectivity changes $(\Delta R/R)/(\Delta R/R_{\text{min}})$ as a function of the pump–probe delay $\Delta t_{\text{p-pr}}$ for fluences between 0.04 and 2.30 mJ cm^{-2}. Dots, experimental data; solid lines, fitted model (see main text). d, Time constant of the initial dynamics as a function of incident excitation fluence. e, Fluence-dependent initial time constant measured by trRHEED. Adapted by permission from Springer Nature Customer Service Centre GmbH: Springer Nature, Nature [67], © 2017, Macmillan Publishers Limited, part of Springer Nature (2017). f, One-dimensional PES model of the optically-induced nonequilibrium phase transition and ballistic order parameter motion.

sensitive to transient electronic excitations as well as coherent phonons and persistent changes in the optical properties of surfaces resulting from phase transitions (see exemplary pump–probe trace in Fig. 9b). In a prototypical OPP experiment, a femtosecond pump pulse in the visible or infrared regime affects the occupation of electronic states close to the Fermi level. For the probe pulse, this influences the rate of allowed optical transitions involving these states and, consequently, the imaginary part of the complex dielectric permittivity ε. Since ε governs the macroscopic reflectivity *R*, transmission *T*, and absorption *A* of the sample, time-resolved measurements of these macroscopic quantities can be used to investigate specific transient changes in electronic or lattice structure [50,140,141]. Furthermore, phase transitions, e.g., between insulating and metallic states, typically involve pronounced changes in the orbital or electronic band structure, respectively. Here, it is not only the change in the occupation of electronic states that affects the permittivity, but the change of the band or lattice structure itself. Whereas OPP is typically used to investigate dynamics in bulk materials, monolayer sensitivity can in principle be achieved, depending on the magnitude of the reflectivity change $\Delta R/R$ introduced by the surface layer and the dielectric function of the substrate [142].

As for the In/Si(111) system, the signals of different optical probes such as Raman spectroscopy [101,102], rotational anisotropy spectroscopy (RAS) [98–100,143] or, in our case, transient reflectivity [51] are dominated by contributions of the In layer, as the Si substrate is not strongly absorbing in the wavelength range of the optical pulses used in these experiments (for example, $\lambda = 800$ nm ($\hbar\omega = 1.55$ eV) or $\lambda = 1030$ nm ($\hbar\omega = 1.2$ eV) in the transient reflectivity measurements). In other words, the absorption coefficient $\alpha = 8{\cdot}10^{-5}$ nm^{-1} for 800 nm light is relatively small, and so is the density of photo-exited carriers of the Si substrate in the vicinity of the surface. Horstmann *et al.* [51], and Frigge *et al.* [67] estimated the total absorption of the In monolayer from experimentally determined quantities to lie between 0.5–1.0 % for the relevant wavelength range, in line with the strong response of ultrathin layers on dielectric substrates observed and modeled in other studies (see, e.g., Ref. [142]). Accordingly, the In surface layer is expected to dominate the optical properties of the system in our experiments.

Our OPP measurements on the Si(111)(8×2)-In surface clearly show periodic modulations of $\Delta R/R$ with delay time, which can be linked to Raman-active low-frequency phonons of the indium monolayer (for details see Ref. [51] and the corresponding Supplementary Material). Here, however, we focus on the initial suppression in the reflectivity traces due to the light-driven phase transition. More specifically, fluence-dependent measurements of the transient reflectivity reveal an acceleration of the initial dynamics from $\tau = 475$ fs at the lowest fluence values to $\tau = 350$ fs for excitation densities $F > 0.5$ mJ cm^{-2} (Fig. 9c and 9d), τ being the time constant of the transition determined from error function fits to the experimental data. While this result qualitatively agrees with the central

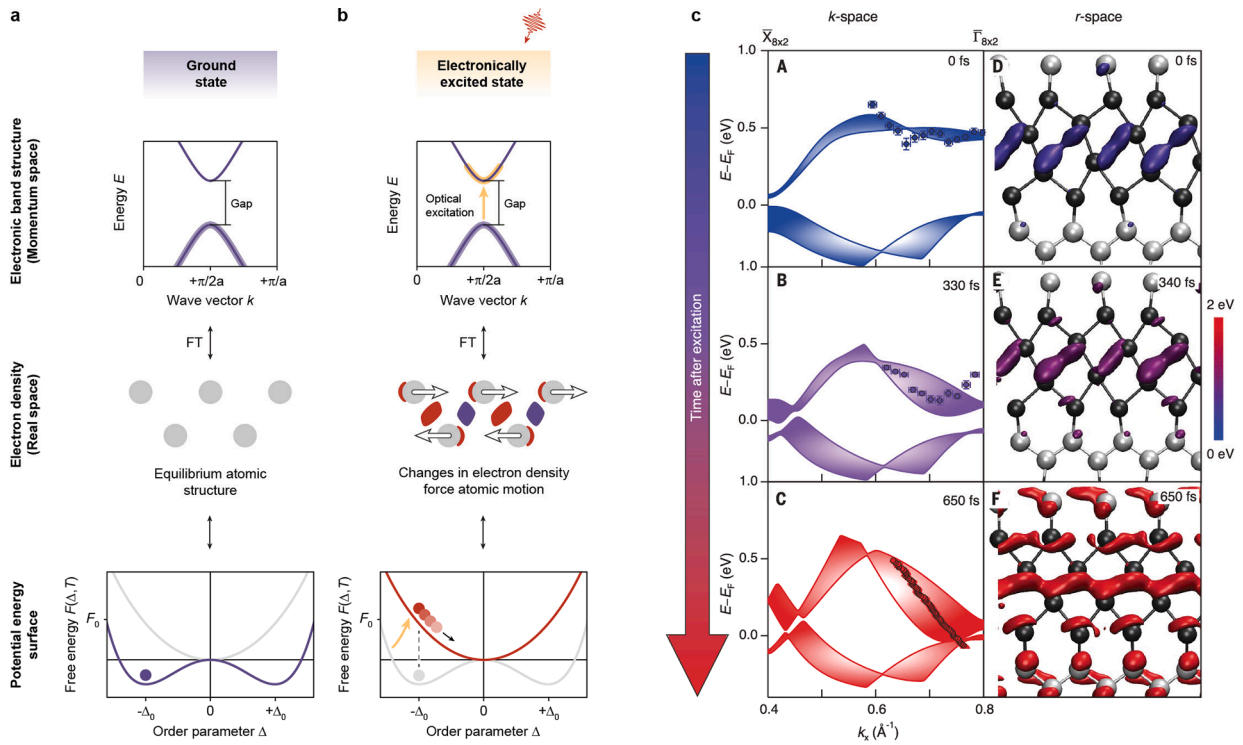

Fig. 10. Coupling of electronic and lattice degrees of freedom in the nonequilibrium (8×2)→(4×1) transition. a,b, Sketch of the microscopic mechanism for the driving of lattice modes by transient electronic excitations. FT, Fourier transform. c, Dynamics of bands and bonds during the insulator-to-metal transition. (A to C) Position of the k-space bands close to the $\Gamma_{(8\times2)}$ point at selected time delays extracted from the trARPES data, overlaid on the calculated LDA band structure (color-filled for clarity). Error bars mark a 95 % confidence level. (D to F) Corresponding real-space dynamics of the orbital, obtained from the Fourier transform of the *k*-space band structures associated with the $\Gamma_{(8\times2)}$ band in (A) to (C). Both the shape of the orbital distribution and the bond strength—indicated by the color scale—change during the phase transition, as a bond across the indium hexagon is formed. Panel c taken from Ref. [63] with permission from AAAS.

results of trRHEED studies (Fig. 9e), i.e., accelerated atomic motion at high excitation densities (Fig. 9f), we also note significant differences between OPP and trRHEED with regard to the threshold fluence and the time constant in the low-fluence regime. A possible explanation for these discrepancies can be given in terms of an additional electronic contribution to the OPP data which rather reflects the time constants $\tau_{trARPES} \approx$ 200–700 fs measured by trARPES at the Γ- and X-points of the band structure [63]. These studies, however, do not report significant changes of the time constant for electronic excitations.

In the following, we will discuss the mechanism behind the acceleration of nuclear motion in the nonequilibrium phase transition, as observed by trRHEED [67] and OPP, in more detail. For this, it is instructive to review mechanisms by which optical excitations drive nuclear motion. Whereas lattice dynamics are often visualized in terms of displacement patterns in real space, the dynamics of electrons or holes, respectively, are typically described in a band structure picture, i.e., in momentum space. Time-resolved ARPES enables a tracking of *k*-dependent transient changes in the occupancy of electronic bands resulting from ultrafast optical transitions. This raises the question as to how electronic excitations observed at specific points in momentum space are reflected in the real-space distribution of charges interacting with the lattice atoms.

Conceptually, in a kinematic diffraction approximation, the positions of the nuclei within the real-space unit cell are connected to the diffraction pattern in momentum space via a Fourier transform. Likewise, the real-space electron density or electronic bonds, respectively, can be inferred from the *k*-dependent band structure [144]. Hence, the (de-)population of electronic states at specific *k*-values in momentum space is associated with a redistribution of charges, or the weakening/strengthening of interatomic bonds in real space, respectively. Nicholson *et al.* [63] used this principle to reconstruct the ultrafast changes in the real-space electron density following optical excitation of the Si(111)(8×2)-In surface from trARPES data (see Fig. 10c). These results enable us to understand, in a real-space picture, how rapid changes of the band structure, e.g., around the Γ-point, initiate directed nuclear motion and thus realize the structural transformation between insulating and metallic states of the indium wires.

For example, the population of conduction band states at the Γ-point and the subsequent energetic downshift correspond to a weakening of interatomic bonds between indium double chains. Following the evolution of the real-space charge density (Fig. 10c, D-F), it becomes clear that the transient redistribution of charges results in Coulomb forces on the nuclei, inducing the displacement pattern of the shear mode (see also Fig. 10a and b). Concerning the accelerated atomic motion observed at high laser fluences *F*, the number of electrons per unit cell excited into relevant states increases with fluence. This causes larger gradients in the charge density distribution, stronger forces, and, accordingly, the acceleration of nuclear motion.

Separating electronic and nuclear dynamics in a Born-Oppenheimer approximation, the structural dynamics are governed by the potential energy surface (PES) (see bottom part of Fig. 10a,b) [145]. The PES represents the free energy of the system in terms of the atomic displacements along specific structural coordinates. Transient electronic excitations quasi-instantaneously change the real space electron density and, in turn, the equilibrium positions of the nuclei, which correspond to minima on the PES. As the nuclei move towards their new equilibrium coordinates in real-space, the order parameter evolves towards the displaced minimum on the PES. The gradient increases with increasing fluence, so that the accelerated motion of the nuclei at high excitation densities can even be described by analogy with classical mechanics, i.e., as a ball rolling down planes of varying gradients. In this scenario, deterministic nuclear motion is facilitated by the direct and virtually exclusive coupling of electronic excitations to shear and rotation modes. This classical picture derived from Landau theory also enables us to understand the optical excitation of coherent phonons in the In/Si(111) system, i.e., its amplitude or Peierls modes.

Generally, different scenarios for coherent phonon generation in photo-exited materials have been identified, the two most prominent being impulsive stimulated Raman scattering (ISRS) and the displacive excitation of coherent phonons (DECP). It has been shown by Garrett *et al.* and Stevens *et al.* that both phenomena can be described within a single theoretical framework, i.e., a combination of two separate Raman tensors [146,147]. While the standard Raman susceptibility tensor accounts for the phonon-induced modulation of the optical susceptibility, the additional tensor characterizes the electrostrictive force acting on the ions [147]. Both tensors have identical real parts and differ only in their imaginary parts. In optically transparent media, both Raman tensors are therefore indistinguishable, and coherent phonon generation is only feasible via the direct interaction of photons with the lattice, i.e., ISRS. In materials with non-vanishing absorption, on the other hand, optically-induced electronic excitations and the subsequent transfer of energy to the lattice by means of electron–phonon coupling can contribute to the excitation of coherent phonons. In this displacive scenario (DECP), the shift of the equilibrium coordinates of the lattice and the subsequent conversion of 'potential' electronic energy into nuclear motion must occur within fractions of the vibrational period to trigger coherent lattice motion. CDW systems represent a prominent model system for this mechanism [34,36,148,149]. Here, promoting electrons across the correlated gap by fs light pulses has been demonstrated to be pivotal for the excitation of characteristic phonons. These structural modes, also known as amplitude or Peierls modes, couple strongly to the populations of electronic states above and/or below the gap [10,15,150], and thus, to the CDW amplitude. Therefore, DECP is considered an important mechanism for the excitation of coherent amplitude modes in CDW materials such as In/Si(111).

In a simplified picture based on Landau theory and DECP, absorption of the pump light results in the excitation of electrons above the CDW gap and, consequently, a quasi-instantaneous displacement of the local minimum of the symmetry-broken phase on the PES, which, in turn, triggers the inertial motion of the nuclei forming the surface layer. Provided a sufficiently low damping or dephasing, e.g., by coupling to other phonon modes, this results in overshooting and subsequent oscillations around the new minimum energy structure. The corresponding real-space motion of the nuclei follows the displacement patterns of shear and rotation modes. As mentioned above, displacive excitation [50] has been shown to be the most common excitation mechanism for Peierls modes and is typically observed after moderate photoexcitation of the CDW ground state [34,148,151]. One should note that strong electron–phonon coupling and the vibronic character of amplitude modes indicate a certain role of non-adiabatic effects, such that despite the practicality of describing the structural evolution as governed by a PES, one should always be careful in the interpretation of

predictions by the Born-Oppenheimer approximation for this system.

Moreover, it is important to consider the potential role of excited carriers in the Si substrate for the nonequilibrium dynamics. Although the phase transition, as observed by ULEED [51,52], trRHEED [43,67,68,109] and trARPES [63–66], is typically initiated by optical excitations well above the band gap of both the In wires and the Si substrate, it is expected that the majority of electronic excitations occur within the In surface layer, as the optical absorption of the Si substrate is small compared with the absorption of the In wires (see also Sec. 4.2). Therefore, while the Si substrate has been shown to influence specific properties of the In/Si(111) system, e.g., the metastability of the supercooled (4×1) phase [86] or the stabilization of the (8×2) phase by means of optical doping [113], at the wavelengths used, the nonequilibrium phase transition is not driven by the diffusion of photo-excited carriers in Si towards the surface [152], but by electronic excitations localized within the In layer. In this respect, the trARPES experiments performed by Nicholson *et al.* [63,64] provide clear evidence for the excitation mechanism underlying the insulator–metal transition, as these studies directly access the transient populations of bands associated with the In layer or the Si substrate, respectively. At the same time, density functional theory (DFT) calculations unequivocally link the phase transition to the optical generation of photoholes and excited electrons in bands associated with the In layer [63,64,67,120,123,124].

4.3. Role of microscopic heterogeneity in the nonequilibrium transition

The impact of microscopic heterogeneity is often not observed or, in part, neglected in spatially averaging experimental studies of surfaces. At the same time, heterogeneity often determines the properties and functionalities of a surface, as exemplified in surface catalysis [153]. In this regard, the In/Si(111) surface once again represents a model system for the investigation of defects, interfaces and finite-size effects in low-dimensional systems. In the insulating phase, we find coexisting insulating (8×2) and supercooled, i.e., metastable metallic (4×1) domains [60,61] separated by atomic-scale interfaces or metal–insulator junctions [154], respectively (see, e.g., Fig. 11c). Moreover, adsorbates or the local dopant concentration of the substrate can affect the local electronic and lattice structure and pin the high-symmetry phase below T_c [89,90]. This raises intriguing questions about the nonequilibrium dynamics of these features following optical excitation. In the following, we demonstrate that the combination of spatially averaging time-resolved techniques such as ULEED, when combined with basic theoretical modeling, enables the investigation of microscopic heterogeneity and its impact on the excitation and relaxation of a transiently excited surface on macroscopic length scales. To this end, we review our results on the signature of heterogeneity in nonequilibrium (8×2)↔(4×1) transition.

In a Landau picture, first-order transitions driven by the quasi-instantaneous reshaping of the PES exhibit a well-defined threshold as a function of electronic or optical excitation density, respectively. At the threshold fluence, the energy barrier between the local minimum of the symmetry-broken and the global minimum of the high-symmetry phase vanishes, and the system evolves into the new ground state. In such models, the level of electronic excitation and, consequently, the transient PES is assumed to be spatially homogeneous. However, this essentially neglects the local modifications of the electronic structure due to inhomogeneities which are expected to result in a spatial distribution of barrier heights on the sample surface.

In ULEED measurements with the mm-sized electron gun, we observe signatures of this distribution in fluence-dependent

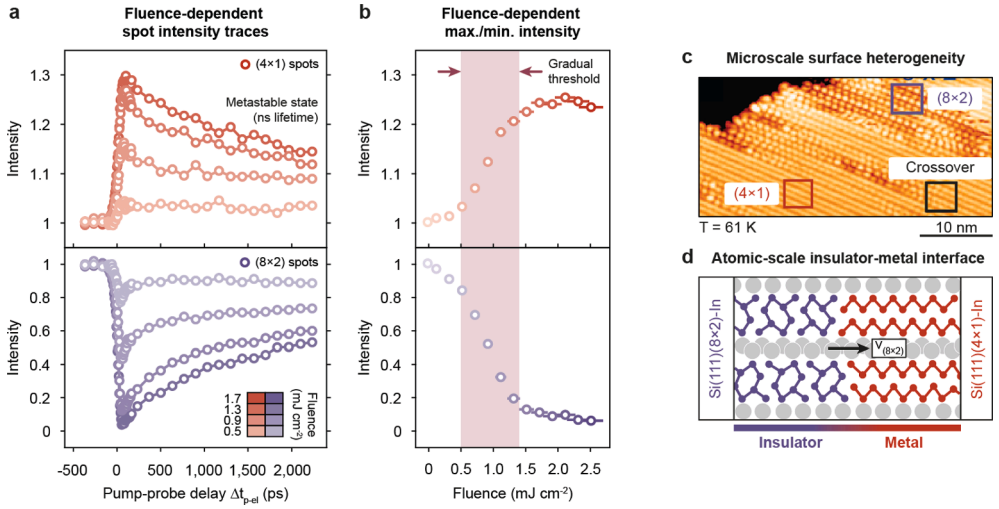

Fig. 11. Signatures of microscopic heterogeneity in ULEED and spatially-resolved measurements. a, Fluence-dependent transient intensities of (4×1) (top) and (8×2) (bottom) diffraction spots recorded by ULEED. b, Fluence-dependent maximum/minimum intensities of (4×1) (top) and (8×2) (bottom) spots recorded around $\Delta t_{p\text{-}el} = 75$ ps. Violet shaded area, threshold region. Panels a,b Taken from Ref. [51]. c, Microscale surface heterogeneity in the form of phase coexistence below T_c as measured by scanning tunneling microscopy. Adapted with permission from Ref. [113]. Copyright 2008 American Chemical Society. d, Schematic of the atomic-scale interface between coexisting (8×2) and (4×1) domains. $V_{(8\times2)}$, phase front velocity relevant for the recovery of the (8×2) ground state following the optical excitation of sample regions into the (4×1) state. (For interpretation of the references to color in this figure legend, the reader is referred to the web version of this article.)

pump–probe measurements of the (8×2)→(4×1) transition (see Fig. 11a). We record both the excitation and relaxation of the metastable (4×1) phase following single-pulse optical excitation and determine the maximum/minimum intensities of (4×1)/(8×2) diffraction spots (typically around $\Delta t_{p\text{-}el}$ = 75 ps) as a function of the incident fluence (Fig. 11b). Herein, the time- and fluence-dependent data are normalized to values before time-zero. Interestingly, instead of a sharp threshold, we find a rather gradual increase of the surface fraction switched into the (4×1) phase with increasing pump fluence [51]. Since the area probed by the electron pulse is homogeneously excited by the pump pulse (see Methods in Ref. [51]), this behavior is indicative of a distribution of local barrier heights for the transition. In contrast to this behavior, with the same experimental setup, a rather sharp threshold was observed for a phase transition in a homogeneous system [135]. Our results also imply that for intermediate excitation densities between 0.5–1.4 mJ cm^{-2}, a variable part of the surface is switched to the (4×1) phase. The mean threshold fluence of $F_{th} \approx 1$ mJ cm^{-2} is in quantitative agreement with trRHEED [67,155] and trARPES [156] studies, as is the critical fluence of $F_c \approx 2$ mJ cm^{-2} for which the entire surface is excited to the (4×1) phase. The interpretation of our data in terms of surface heterogeneity is supported by a number of studies on atomic-scale defects affecting the local barrier height for the transition [61,88,114,127,154]. The heterogeneity of the Si (111)(8×2)-In surface has also been investigated by STM [60,154,157] and Raman spectroscopy [101] studies. The residual intensity of metallic bands observed in trARPES below T_c [156] further corroborates our model.

Next, we analyze the subsequent relaxation of the system to the ground state. As a main observation, we find a relatively fast recovery of spot intensities within 100 ps after excitation at low and intermediate fluence values (Fig. 11a). At later delays, however, the relaxation considerably slows down, as evidenced by the persistent suppression/enhancement of diffraction spots even after several nanoseconds. Our observations cannot be described in terms of a single exponential decay of the excited state population (see, e.g. Ref. [68]). Likewise, a transient Debye-Waller suppression can be ruled out in this low-fluence regime [67,109]. This calls for further investigations of the relaxation dynamics with improved temporal resolution using the micrometer-sized ultrafast electron gun.

Fig. 12a shows the delay-dependent intensities of (8×2) diffraction spots recorded with the micrometer-sized gun for three incident laser fluences between 0.46–1.18 mJ cm^{-2}, i.e., in the threshold regime. Focusing on the recovery dynamics, we find that intensity traces recorded at different pump fluences differ considerably. More specifically, at the lowest fluence value of 0.46 mJ cm^{-2} (top, light violet), the (8×2) spot intensity recovers by about 50 % within the first 30 ps after the initial suppression, followed by a significantly slower relaxation on a nanosecond timescale. A similar trend is observed at higher fluences, but the persisting signal suppression is a function of the fluence F with 40/65/85 % of the initial suppression remaining after 50 ps for 0.46/0.85/1.18 mJ cm^{-2}.

We discuss these observations in the light of the model for the recovery of the Si(111)(8×2)-In surface proposed by Hafke *et al.* [68]: Due to its first-order nature, the transition from the photo-excited (4×1) to the (8×2) ground state occurs by analogy with a 'falling row of dominoes', i.e., unit cell by unit cell [43]. Assuming that step edges (and adsorbates) function as seeds for the return of a homogeneously switched surface to the ground state, a characteristic velocity v_{rec} = (100 ± 40) m/s = (0.1 ± 0.04) nm/ps for the motion of (4×1)/(8×2) domain boundaries was determined by recording the distribution of terrace widths Γ on a Si(111) surface in

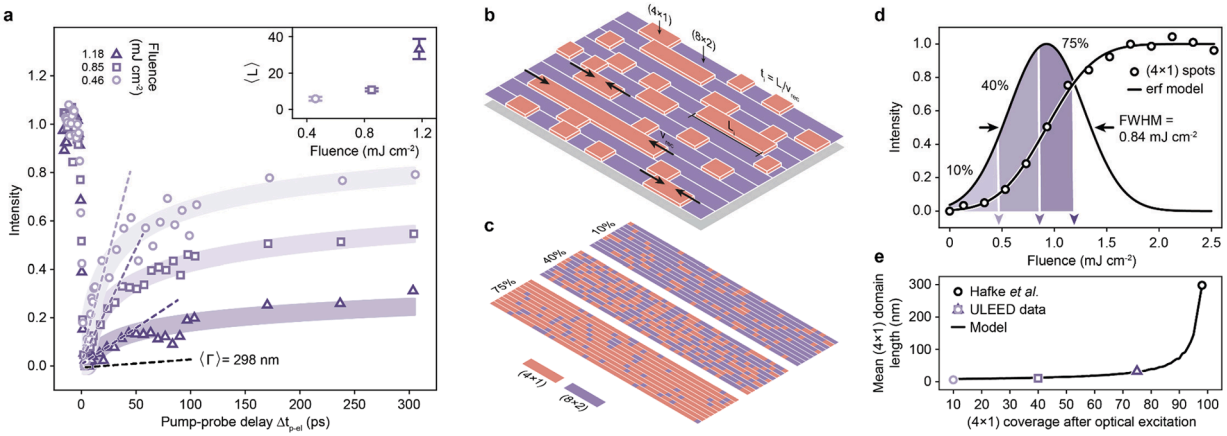

Fig. 12. Relaxation of the metastable (4×1) state to the (8×2) state and heterogeneity of the surface after moderate optical excitation. a, Delay-dependent (8×2) spot intensities for different excitation fluences reveal a partial relaxation of the excited state within ≈ 50 ps and a subsequent slowdown of the recovery dynamics. The data is corrected by the maximum suppression ($\Delta t_{p\text{-}el} \approx 3$ ps) and normalized to values before $\Delta t_{p\text{-}el} = 0$. Shaded traces in background, stretched exponential fits serving as guide to the eye. Dashed colored lines, linear models fitted to the data for $\Delta t_{p\text{-}el}$ to estimate the initial mean (4×1) domain length. Dashed black line, reference value from Ref. [68]. Inset, calculated mean domain length as a function of excitation fluence. b, Model of surface heterogeneity after weak optical excitation roughly corresponding to $F = 0.85$ mJ cm^{-2} ($A_{(4\times1)}/A_{tot} \approx 40$ %). v_{rec}, phase front velocity of the (4×1)→(8×2) transition; L_i, length of domain i; t_i, lifetime of the respective (4×1) domain. c, Model of the optically excited surface assuming an individual switching efficiency of 10/40/75 % for each unit cell. d, Gaussian distribution of barrier heights for the (8×2)→(4×1) transition inferred from the fluence-dependent (4×1) diffraction spot intensity (black dots, see also Fig. 5.2b). Black line, error function model fitted to the experimental data. Shaded areas indicate the fraction of the surface switched for excitation fluences of 0.46, 0.85 and 1.18 mJ cm^{-2} in microgun pump–probe experiments. e, Mean (4×1) domain length ⟨L⟩ as a function of the (4×1) reconstructed fraction of the surface calculated from the model in (c). Dots, domain lengths extracted from trRHEED and ULEED measurements at different fluences. The model curve has been normalized to the value for the mean domain size yielded by Hafke et al. [68] in the case of a completely switched surface.

photoemission electron microscopy (PEEM) [68]. In this picture, the time it takes for a particular domain i of length Γ_i to completely transform back to the ground state is given by $t_i = \Gamma_i/v_{rec}$ (see also Fig. 12b). For a homogeneously switched surface exhibiting a geometric distribution of barrier heights, and a mean value $\langle\Gamma\rangle_i = 298$ nm, this model reproduces the exponential decay of the metastable phase with a time constant of 3 ns, in agreement with trRHEED data [68].

ULEED measurements now indicate that for fluences below $F_{tot} = 1.7$ mJ cm^{-2}, only a fraction of the (8×2) surface is switched to the (4×1) state. We speculate that the domains switched at low fluences exhibit particularly shallow barriers for the transition into the (4×1) structure. By fitting an error function model to the fluence-dependent spot suppressions from Fig. 11b, we obtain a Gaussian distribution of barrier heights with a FWHM of 0.84 mJ cm^{-2} for the (8×2)→(4×1) transition (Fig. 12d). This allows us to estimate the (4×1) surface fraction after optical excitation for a given excitation fluence (see shaded areas in Fig. 12d) in. Herein, we assume that the effective barrier for the transition is, to some extent, locally altered by surface defects, dopant atoms, and/or boundaries between (8×2) and supercooled (4×1) domains. Based on our model, we estimate a (4×1) coverage of 10/40/75 % for $F = 0.46/0.85/1.18$ mJ cm^{-2} in the above fluence-dependent data.

A comparison of the excited state lifetimes for partially and completely switched surfaces in Refs. [68,155] now points to a spatially heterogeneous distribution of individual (4×1) domains within the illuminated area for $F < F_{tot}$. Fig. 12b shows a schematic representation of such a partially transformed surface for $A_{(4\times1)}/A_{tot} = 40$ %, where $A_{(4\times1)}/A_{tot}$ refers to the surface fraction switched into the (4×1) phase. It is reasonable to assume that the distribution $P(L)$ of domain lengths L is no longer determined by the distribution $P(\Gamma)$ of terrace widths Γ alone. Instead, for a partially switched surface, the mean (4×1) domain size $\langle L\rangle$ may be significantly smaller than $\langle\Gamma\rangle$, leading to an overall faster recovery. By comparing the initial recovery rates in our experiments (see linear model fitted to the fluence-dependent (8×2) spot intensities for $\Delta t_{p\text{-}el} < 30$ ps in Fig. 12a) to the model of Ref. [68] for a homogeneously switched surface (dashed black line), we estimate the mean domain size to be (5 ± 1) nm for $A(4\times1)/A_{tot} = 10$ % and (33 ± 7) nm for $A(4\times1)/A_{tot} = 75$ % (see inset in Fig. 12a and Fig. 12e).

Moreover, a simple numerical model of the surface can be used to further relate these results to the results of Hafke *et al.* To this end, we assume an independent switching probability $P_s = A(4\times1)/A_{tot}$ for each unit cell and calculate the spatial distribution of (4×1) and (8×2) domains on a one-dimensional grid for different values of P_s (Fig. 12c). From this, we extract the mean (4×1) domain length $\langle L\rangle$ as a function of the (4×1) coverage (Fig. 12e). A comparison of the domain lengths inferred from the slope of the delay-dependent (8×2) spot intensities in Fig. 12a (coloured dots in Fig. 12e) with the predictions of this simple model shows good agreement, suggesting that surface heterogeneity controls the relaxation to the ground state.

We note that at large pump–probe delays, the slope of the data in Fig. 12a decreases significantly and approaches the value found by Ref. [68]. As a possible explanation for this behavior, the surface exhibits a non-negligible fraction of particularly long (4×1) domains even for a weak optical excitation. Alternatively, the long-term recovery of the ground state of the indium wires may be influenced by long-lasting photodoping and heating effects in the substrate. Here, the excitation of carriers in the silicon substrate could lead to the formation of a space-charge region in the vicinity of the surface and a subsequent charge transfer to the indium monolayer. In this regard, STM measurements under cw-laser illumination showed evidence for such an effect and investigated the possibility to stabilize

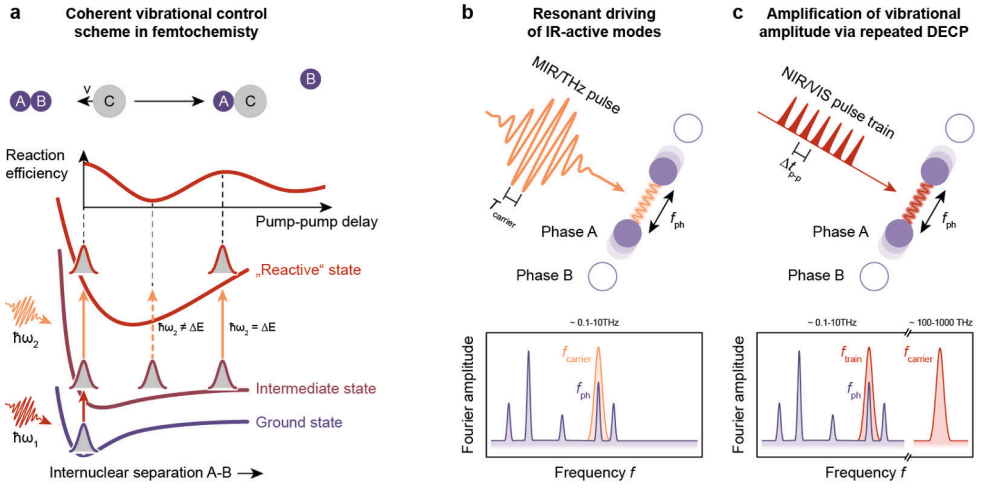

Fig. 13. Optical control enabled by vibrational degrees of freedom of molecules and solids. a, Coherent vibrational control scheme in femtochemistry. A first optical stimulus by a femtosecond light pulse excites the A-B dimer from its ground state to an intermediate state and launches a vibrational wave packet. By tuning the wavelength of a second excitation pulse so that the transition into the reactive state of the dimer is only possible at two points of the vibrational trajectory, the reaction efficiency can be made a function of the double-pulse delay. Adapted from Ref. [165]). b, Schematic of optical control over solids via the resonant driving of infrared-active lattice modes. The carrier frequency of the excitation pulse is matched to the phonon frequency (bottom). c, Control scheme harnessing the repeated displacive excitation and amplification of coherent phonons by optical pulse trains. Whereas the frequency of the pulse train is matched to the phonon frequency, the carrier frequency can be orders of magnitude higher, e.g., in the optical regime. Note that the optical excitation interacts only indirectly with the lattice via optically-induced electronic excitations which, in turn, strongly couple to the relevant phonon mode.

the (8×2) phase below T_c by photodoping [113]. In summary, the results of ULEED not only demonstrate that microscopic surface heterogeneity can drastically affect nonequilibrium structural dynamics, but also that spatially averaging techniques can, to some extent, investigate these phenomena in combination with tailored measurement schemes and theoretical modeling.

5. Coherent vibrational control

5.1. Coherent control: From molecules to solids

Up to this point, we have focused on the probing of ultrafast structural dynamics following single-pulse optical excitation of the Si (111)(8×2)-In surface. While the results of ULEED add to key observations made by trRHEED [43,67,68,109] and trARPES [63–66] on the same system, they also shed new light on the role of surface heterogeneity in the transition as well as the subsequent relaxation, stimulating further experiments in this direction. In this sense, ULEED joins a series of time-resolved diffraction [33,44,67,132,158] and imaging [29,31] studies that have contributed to our understanding of nonequilibrium structural dynamics in solids and surfaces. However, based on a sound understanding of the fundamental dynamics in condensed matter systems, the focus of the field is continuously shifting from mere observation to the active, optical control of material properties far from equilibrium [24,159,160]. In this respect, our system represents a promising target, because of its quasi-one-dimensional character, a Peierls-like metal–insulator transition, and a particularly strong coupling of decisive phonons to optical excitations. Thus, in the next step, we go beyond observing the (8×2)→(4×1) transition and investigate the possibility to exert coherent control over it.

Such all-optical control of matter is pursued in various scientific fields including ferroics [161–163], magnetism [38] and especially femtochemistry [164]. In the latter case, coherences in the electronic and vibrational degrees of freedom of molecules are harnessed to control the efficiencies of chemical reactions. Fig. 13a shows the schematic of a prototypical femtochemistry experiment featuring the coherent vibrational control of a 'harpoon reaction' of the AB + C ⟶ AC + B type [165]. A first ultrashort light pulse (red) excites the AB dimer from its ground into an intermediate state and launches a vibrational wave packet, i.e., an oscillation of the internuclear separation (A–B). Depending on the vibrational phase at the time of a second optical excitation (orange), the dimer is either excited to a reactive state facilitating the reaction or remains in its intermediate state. This way, the reaction efficiency becomes a function of the double-pulse optical delay $\Delta t_{p\text{-}p}$, mediated by vibrational coherence.

A transfer of such control schemes to solids requires the efficient generation of coherent phonons and optical control over their amplitudes. Resonant driving of IR-active phonons (Fig. 13b) by intense mid-infrared or THz fields has proven a powerful tactic to transiently manipulate materials properties and to induce phase transitions into metastable or superconducting states [161–163,166–168]. However, this approach does not necessarily harness phonon coherences. In an alternative approach, Weiner,

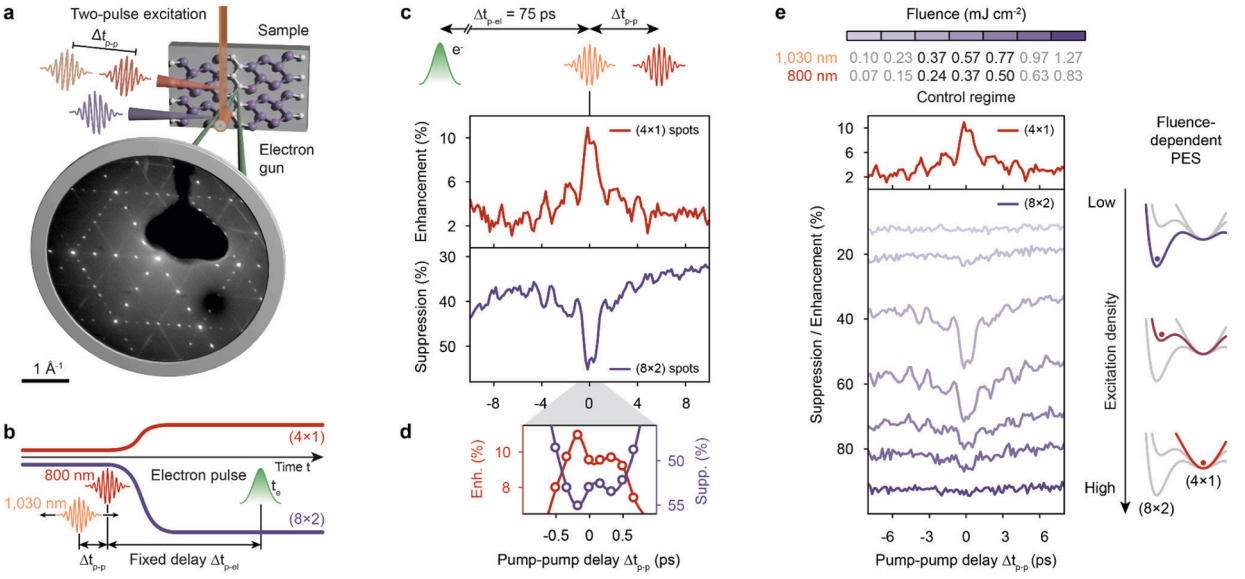

Fig. 14. Coherent vibrational control of the (8×2)→(4×1) transition. a, Schematic of the experimental setup for ULEED in combination with two-pulse optical excitation. b, Sketch illustrating the pulse sequence in the time domain. Red (orange), 800 (1030) nm optical pump pulses; green, electron pulse. c, Suppression/enhancement of the integrated (8×2)/(4×1) diffraction spot intensity as a function of the double-pulse delay $\Delta t_{p\text{-}p}$ for incident fluences $F_{1030} = 0.37$ mJ cm^{-2} and $F_{800} = 0.24$ mJ cm^{-2}. The signal is normalized to values recorded for $F_{1030} = F_{800} = 0$ and $\Delta t_{p\text{-}el} = 75$ ps. d, (8×2)/(4×1) spot suppression/enhancement close to $\Delta t_{p\text{-}p} = 0$. e, (Right) Double-pulse traces recorded for different pump fluences F_{1030} and F_{800}. (4×1) trace identical to b. (Left) 1D model of the PES after first optical excitation for low (top), medium (middle) and high (bottom) excitation density or pump fluence, respectively. Colored dots, position of the order parameter. Panel a and d (For interpretation of the references to color in this figure legend, the reader is referred to the web version of this article.)
Adapted from Ref. [51].

Nelson *et al.* [169–171] investigated the use of optical pulse sequences to excite coherent phonons in materials by means of DECP or impulsive stimulated Raman scattering (ISRS), in order to repeatedly amplify the vibrational amplitude. To this end, not the carrier frequency of the optical excitation, but the delay between successive light pulses is matched to the phonon frequency (see Fig. 13c). In contrast to the resonant driving of lattice modes, this approach necessitates coherence times exceeding the phonon period.

At the same time, active control over the efficiency of a phase transition via phonons requires the energy stored in the coherent vibrational motion to be comparable to the barrier separating the two states within a certain surface area. In this regard, the gradual threshold for the (8×2)→(4×1) transition suggests a spatial distribution of energy barriers between (8×2) and (4×1) configurations (see Fig. 11b and related discussion). Within the intermediate fluence regime, the transition is susceptible to weak perturbations, given the role of electronic excitation in shaping the PES and, consequently, barrier height. Here, a large fraction of the remaining (8×2) domains likely exhibit a sufficiently lowered but non-vanishing barrier immediately after moderate optical excitation. Furthermore, the Peierls-like nature of the transition as well as the key role of displacive excitation in driving the underlying structural changes on a femtosecond timescale suggest that the creation of such an excited (8×2) phase is accompanied by the generation of vibrational coherences.

The missing signatures of coherent shear and rotation phonons in earlier studies of the nonequilibrium phase transition were previously attributed to a rapid energy transfer of these modes to lower-lying surface and bulk phonons [67,108]. Moreover, the absence of coherent oscillations in trRHEED featuring single-pulse optical excitation could also be explained by a relatively small impact of shear and rotation distortions on the structure factor in these types of experiments. Interestingly, however, trARPES measurements point to a highly non-thermal distribution of optical phonons after photo-excitation and a bottleneck for the cooling of the electronic system determined by electron–phonon and phonon–phonon coupling [64]. This raises the question of whether long-lived vibrational coherence, though hard to detect directly via its impact on the structure factor, exists in the (8×2)→(4×1) transition. If so, it could potentially be harnessed to exert coherent control over the phase transition.

5.2. Coherent control over the switching efficiency

A promising way to investigate the existence and potential impact of vibrational coherence in the (8×2)→(4×1) transition is to amend our diffraction experiments by tailored optical excitation. Specifically, to explore the applicability of coherent vibrational control schemes from femtochemistry to solids, we combine ULEED with optical pulse sequences (Fig. 14a) [51]. In a first step, we aim to manipulate the switching efficiency

$$E_s\left(\Delta t_{p-p}\right) = 1 - \frac{I_{8\times2}\left(\Delta t_{p-p}\right) - \left\langle I_{8\times2}\left(\Delta t_{p-p} > \Delta t^*_{p-p}\right)\right\rangle}{\left\langle I_{8\times2}\left(\Delta t_{p-p} > \Delta t^*_{p-p}\right)\right\rangle}$$

of the transition between the (8×2) and the (4×1) phase close to its threshold by means of double-pulse excitation. Here, $I_{8\times2}$ is the integrated intensity of (8×2) diffraction spots, $\Delta t_{\text{p-p}}$ is the delay between two optical excitations, and $\Delta t^*_{\text{p-p}}$ is significantly longer than the coherence time of the relevant shear and rotation phonons. The pulse sequence in these experiments is visualized in Fig. 14b. Instead of a single intense optical pulse, we harness a pair of weaker pump pulses (P1, $\hbar\omega = 1.2$ eV; P2, $\hbar\omega = 1.55$ eV) with variable delay $\Delta t_{\text{p-p}}$ to drive the transition and probe the resulting structure or 'reaction product', respectively, by ULEED at a later time of $\Delta t_{\text{p-el}} = 75$ ps. This way, ULEED can be harnessed to determine the efficiency of the (8×2)→(4×1) transition or, in other words, the surface fraction switched to the metastable (4×1) state.

Fig. 14c depicts the variation in intensities of (4×1) and (8×2) diffraction spots, indicating enhancement or suppression, as a function of the double pulse delay $\Delta t_{\text{p-p}}$. The incident fluences for this analysis are $F_{1030} = 0.37$ mJ cm^{-2} and $F_{800} = 0.24$ mJ cm^{-2}. We observe that the characteristic pattern of the metastable state, which manifests as a mirror-like suppression or enhancement of (8×2)/(4×1) diffraction spot intensity, strongly depends on $\Delta t_{\text{p-p}}$. Specifically, when the combined fluences fall within the intermediate range of 0.5–1.4 mJ cm^{-2} (refer to Fig. 11b and Fig. 14e), prominent oscillations with a period of approximately 1–2 ps are observed on both sides of double-pulse overlap ($\Delta t_{\text{p-p}} = 0$), exhibiting opposite behavior for the (4×1) and (8×2) spots. Notably, we also observe a significant enhancement or suppression signal around $\Delta t_{\text{p-p}} = 0$, which we attribute to transient electronic excitations reshaping the potential energy landscape. Additionally, an intriguing observation is that the maximum enhancement or suppression is not observed at $\Delta t_{\text{p-p}} = 0$, but rather at $\Delta t_{\text{p-p}} = 300$ fs, roughly corresponding to one quarter of the rotation mode period ($T_{\text{rot}} = 1.2$ ps). In terms of the maximum effectiveness of the double-pulse control scheme, we determine a modulation amplitude of up to 4 % based on the fluence-dependent analysis shown in Fig. 14c.

The observed oscillations provide clear evidence of a coherent response in the signal, and the frequency range of the signal modulation (<1 THz) indicates that it originates from vibrational dynamics. Specifically, the coherent motion of atoms, triggered by the first pulse, influences the efficiency of the switching process after the second pulse. Considering the resonant excitation conditions ($\hbar\omega > \Delta E_g$) and drawing from previous experimental and theoretical studies, we propose that the DECP is responsible for generating these coherent phonons in the system. To further investigate this effect, we recorded switching efficiency traces at various combined fluences F_{comb} ranging from 0.17 mJ cm^{-2} (light violet) to 2.10 mJ cm^{-2} (dark violet). The results reveal that coherent oscillations are only present within an intermediate fluence range, specifically between 0.61–1.27 mJ cm^{-2} (Fig. 14e). The data is normalized to peak intensities measured at $\Delta t_{\text{p-el}} = 75$ ps and $F_{1030} = F_{800} = 0$ mJ cm^{-2}. At lower or higher fluences, the oscillations are either significantly dampened or completely absent.

We now discuss these results within the one-dimensional potential energy surface (PES) model for the transition [43,67,86].

Moreover, we take into account the surface's heterogeneity, specifically the coexistence of (8×2) and metastable (4×1) domains, by assuming a distribution of local barrier heights for the (8×2)→(4×1) transition. When the excitation densities are low ($F_{comb} < 0.38$ mJ cm^{-2}, Fig. 14e), the initial pump pulse only converts less than 10 % of the surface into the (4×1) phase. Whereas these domains likely exhibit initially low barrier heights, the remaining (8×2) domains have relatively high barriers towards the (4×1) phase. Consequently, while the first pump pulse may excite coherent phonons of the (8×2) structure, their vibrational amplitude is insufficient compared to the remaining barrier, and thus it does not significantly influence the transition process. However, at high excitation densities ($F_{comb} > 1.6$ mJ cm^{-2} in Fig. 14e), the first pulse transforms the majority of (8×2) domains into the metastable state, resulting in a significant reduction of the switchable fraction of the surface for the second pulse. Only in the control regime (middle), where changes in energy caused by coherent vibrational motion in the excited (8×2) phase are comparable to the energy barrier $\Delta\Delta E_{EBarrier}$ for a sufficiently large portion of the surface, the impact of vibrational coherence on the transition can be observed by spatially averaging experiments.

These observations directly link our work to Refs. [67] and [108], which find a critical damping of shear and rotation modes at high excitation densities. For this fluence regime, our measurements explain the absence of coherent amplitude motion and a corresponding contribution to diffraction peak intensities. Future ultrafast electron diffraction experiments with sufficiently high temporal resolution could be able to directly observe phonon coherences in experiments with only a single optical excitation, provided a sufficiently high signal-to noise ratio for (8×2) diffraction spots, and a measurable impact of coherent atomic motion on the structure factor.

5.3. Decisive modes and ballistic control

The crucial role of vibrational coherence in controlling the transition is demonstrated by the periodic modulation observed in the double-pulse traces. However, the origin of these coherent oscillations prompts further investigation. Here, we first identify the lattice modes that contribute to this effect. Subsequently, we discuss the mechanism through which these phonons enable control over the transition efficiency. To this end, we conduct a Fourier analysis of the relative switching efficiency in a double-pulse experiment with

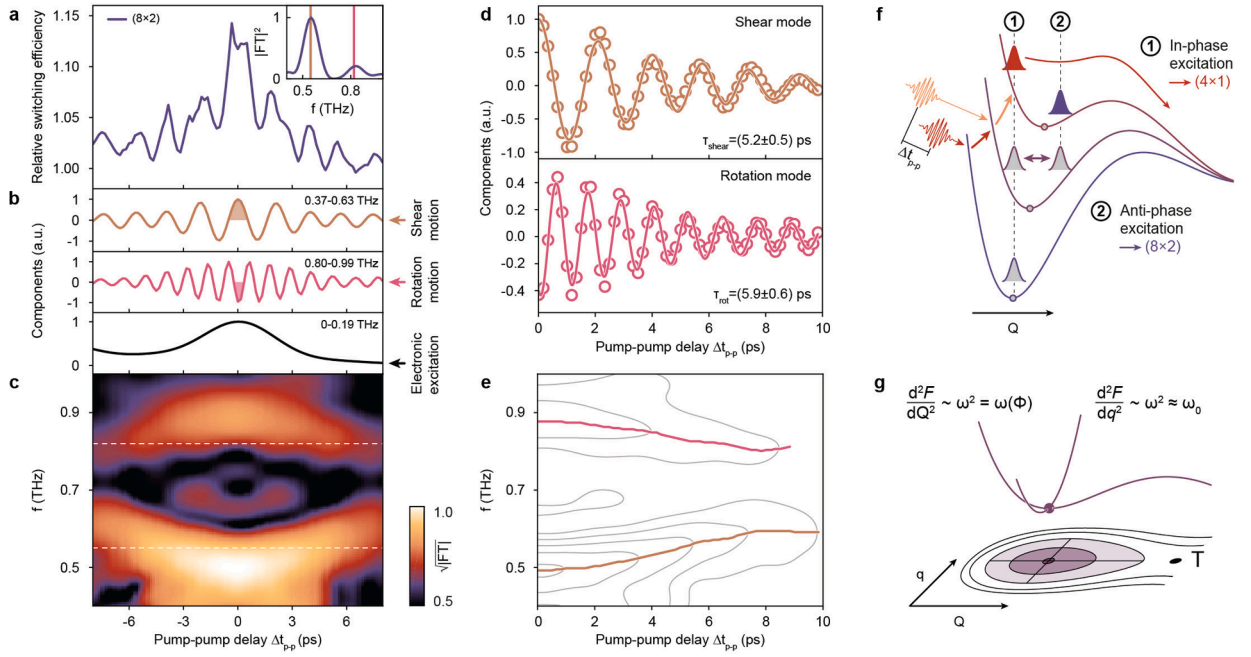

Fig. 15. Frequency-analysis of the switching efficiency, transient frequency shifts and ballistic control mechanism. a, Delay-dependent relative switching efficiency for $F_{1030} = 0.32$ mJ cm^{-2}, $F_{800} = 0.21$ mJ cm^{-2}. Inset, spectral density of switching efficiency; vertical lines represent the frequencies of structural antisymmetric shear and hexagon rotation modes. FT, Fourier transform. b, Fourier-filtered contributions of different frequency components. Golden and pink shaded regions indicate the distinct initial phases. a.u., arbitrary units. c, Short-time Fourier transform of the dataset in a, revealing a pronounced softening/hardening of the shear/rotation component close to $\Delta t_{p\text{-}p} = 0$. d, Shear (top) and rotation (bottom) frequency components of the relative switching efficiency trace in a (dots), and damped oscillator models (solid lines) fitted to the data. e, Delay-dependent dominant frequency of shear (golden) and rotation (pink) modes as a function of $\Delta t_{p\text{-}p}$ (dataset in a). Grey contour lines, STFT from c. f, Ballistic control scheme: A first optical excitation induces coherent vibrational motion in the excited (8×2) potential via DECP (middle). A second optical excitation delayed by $\Delta t_{p\text{-}p}$ either increases or decreases the vibrational amplitude, depending on the momentary vibrational phase. For a nonvanishing barrier after the second excitation, kinetic energy contributes to overcoming the barrier into the (4×1) state (top). This mechanism is feasible for modes along the reaction coordinate Q. g, Schematic of the frequency softening of structural modes pointing towards the transition state. T, transition state. Panels a, b, c, and f taken from Ref. [51]. (For interpretation of the references to color in this figure legend, the reader is referred to the web version of this article.)

$F_{1030} = 0.32$ mJ cm^{-2} and $F_{800} = 0.21$ mJ cm^{-2} (Fig. 15a), associating the two dominant frequency contributions with modes of the (8×2) structure. The presence of a low-frequency feature at $f = 0.55$ THz indicates the involvement of the antisymmetric shear mode, which governs the shearing of adjacent indium chains and is linked to the up/down movement of the m_1 band around the zone center ($\Gamma_{(8\times2)}$ point) as well as the charge transfer to the m_2/m_3 bands. On the other hand, the high-frequency feature is attributed to the hexagon rotation mode at $f = 0.82$ THz, responsible for the Peierls dimerization along the outer indium rows and its coupling to the gap at the Brillouin zone boundary ($X_{(8\times2)}$ point).

Interestingly, the individual contributions of shear and rotational motion on the delay-dependent transition efficiency, gained by an inverse Fourier transform of the respective frequency component, exhibit distinct initial phases (Fig. 15b). We note, however, that pump–probe and pump-pump–probe experiments yield different observables. More specifically, and in contrast to pump–probe measurements which provide direct access to the amplitudes and initial phases of structural modes, the observable in ULEED pump-pump–probe experiments is the phase transition efficiency, i.e., the double-pulse-delay-dependent intensity of (8×2) diffraction peaks after the transition. Therefore, it is not straightforward to draw direct conclusions about the initial phases of shear and rotation modes, as the intensity traces in Fig. 15a and b do not represent the time-dependent amplitudes but rather the impact of the momentary mode amplitude after the second excitation on the phase transition efficiency. Assuming displacive excitation as the primary excitation mechanism of shear and rotation modes, the transition efficiency is increased/decreased when the shear/rotation mode is initially excited to maximum amplitude. While this accounts for the peculiar behavior of the phase transition efficiency around $\Delta t_{p\text{-}p} = 0$ (Fig. 14d), the reasons behind the different roles of shear and rotation motion in controlling the transition require further investigation (see below). In addition to examining vibrational coherence, Fourier filtering allows for the separation and investigation of electronic contributions to the transition efficiency (Fig. 15b, bottom, 0–0.19 THz). In particular, the enhanced switching efficiency resulting from electronic excitation can be explained by a transient deformation of the one-dimensional potential energy surface (PES), enabling the switching of (8×2) domains towards the (4×1) state even with relatively small energy barriers. The extracted lifetime of electronic excitation (approximately 3 ps) aligns with trARPES data [63,64].

Next, we examine the evolution of shear and rotational phonon frequencies as a function of the double-pulse delay. The investigation of such frequency changes is highly useful as it provides insights into the potential energy surface (PES) of the transition and the significance of specific modes, especially their orientation relative to the reaction pathway. In particular, modes pointing towards a transition state on the PES generally soften with increasing electronic excitation or temperatures approaching T_c, respectively (Fig. 15g). This can be understood by considering the continuous transformation between the potential energy surfaces of broken and high-symmetry states, which involves an increasingly shallower (8×2) free-energy minimum. Furthermore, at elevated temperatures, the magnitude of lattice fluctuations, including shear and rotation modes, increases, and the anharmonicity of the local potential becomes significant. This effect is expected to be more pronounced near the transition state, which represents a saddle point on the PES. To analyze the frequency shifts of shear and rotation modes as a function of double-pulse delay, we analyze the data presented in Fig. 15a with a short-time Fourier transform (STFT, also referred to as 'time-windowed Fourier transform' in the literature [172]). Specifically, we evaluate the Fourier transform of the delay-dependent relative switching efficiency $E_S(\Delta t_{p\text{-}p})$ within a super-Gaussian window $F_{filt}(\Delta t_{p\text{-}p}, \Delta t_{shift})$ (refer to Ref. [51] for detailed information) in the time domain. This involves calculating the product $E_s(\Delta t_{p\text{-}p}) \cdot F_{filt}(\Delta t_{p\text{-}p}, \Delta t_{shift})$ for values of $-\Delta t_{p\text{-}p}^* < \Delta t_{shift} < \Delta t_{p\text{-}p}^*$. The resulting spectral density is depicted as a function of double-pulse delay and frequency in Fig. 15c. Notably, a significant softening is observed for the shear feature around double-pulse overlap, whereas the rotation mode undergoes considerable hardening (the dominant frequencies of shear (golden) and rotation (pink) modes are also highlighted in Fig. 15e). From this observation, we propose that shear distortions serve as the primary 'reaction coordinate' Q pointing towards the transition state, whereas rotational motion plays a secondary role in the transition.

In addition to the transient softening and hardening of the observed coherent phonons, an analysis of the respective lifetimes τ_{shear} and τ_{rot} is interesting with regard to trARPES results on momentum-resolved population dynamics [64]. Assuming a linear increase (decrease) in shear (rotation) frequency over time, i.e., $\omega = \omega(\Delta t_{p\text{-}p}) \approx (\Delta\omega/\Delta\,(\Delta t_{p\text{-}p})) \cdot \Delta t_{p\text{-}p}$, a damped oscillator model can be fitted to the individual frequency contributions from Fig. 6.4a to estimate τ_{shear} and τ_{rot}:

$$\xi(\Delta t_{p-p}) = \xi_0 \, exp\left(-\frac{\Delta t_{p-p}}{\tau}\right) \cdot \, cos\left(\omega(\Delta t_{p-p})\Delta t_{p-p} - \phi\right)$$

Here, ξ is the vibrational amplitude and ϕ the initial phase of the coherent oscillation. From the fits, we extract lifetimes of $\tau_{shear} = (5.2 \pm 0.5)$ ps for the shear and $\tau_{rot} = (5.9 \pm 0.6)$ ps for the rotation mode (see also Fig. 15d). This indicates that the decay of optically-triggered vibrational coherence in shear and rotational modes occurs on a similar timescale as the electronic temperature. Nicholson *et al.* [64] proposed a mechanism for energy relaxation following ultrafast optical excitation. They suggest that high-energy optical phonons act as a bottleneck for electron cooling, based on a thermal model of electron population dynamics and the observation of a sustained elevated electron temperature beyond 1 ps. According to their hypothesis, electronic energy preferentially transfers to high-energy optical phonons, which are strongly coupled to the electronic system but weakly coupled to lower-energy phonons. Nicholson *et al.* predict a highly nonthermal distribution of these phonons, which decay on a timescale of a few ps due to phonon–phonon coupling with lower-lying modes. The observation of coherent optical shear and rotation phonons in ULEED supports this hypothesis. Moreover, the corresponding lifetimes τ_{shear} and τ_{rot} obtained from the Fourier-filtered contributions to the switching efficiency suggest that the energy stored in shear and rotation motion is transferred to the underlying lattice within approximately 6 ps, as confirmed by trRHEED measurements of the maximum lattice temperature [67,109].

These findings provide evidence for the presence of long-lasting vibrational coherence following optical excitation of the Si(111) (8×2)-In surface. However, it is still unclear how this coherent atomic motion contributes to controlling the efficiency of the (8×2)→

(4×1) transition in double-pulse experiments. Drawing on the insights from ULEED and OPP, as well as the overall understanding of the nonequilibrium transition established in previous works [63,67], we propose a control mechanism that relies on the energy stored within the coherent motion of lattice atoms. Specifically, considering the ballistic nature of the (8×2)→(4×1) transition and the influence of DECP, we suggest that the kinetic energy stored in the inertial motion of the order parameter plays a role in overcoming a sufficiently lowered barrier (refer to Fig. 15f). In this "ballistic control" scenario, the first optical stimulus excites coherent shear and rotation phonons through displacive excitation. By applying an in-phase excitation with a second pulse along the 'reaction' coordinate *Q*, the effect of DECP is maximized, the vibrational amplitude is increased, and barrier crossing towards the (4×1) phase is facilitated (1). Conversely, an anti-phase excitation leads to vibrational de-excitation of the system, resulting in insufficient kinetic energy to transition, thereby remaining in the (8×2) minimum (2). In a corresponding real-space depiction, the second pulse either adds additional mechanical stress to the system (1) or reduces it (2) by weakening or strengthening different indium-indium bonds, consequently shifting the equilibrium positions of atoms (refer to Fig. 10f).

In this picture, the abstract coordinate *Q* in Fig. 15f does not necessarily refer to a single phonon mode at a specific wave vector but rather to a combination of those lattice distortions that transform the (8×2) into the (4×1) structure, here, the antisymmetric shear and the hexagon rotation modes. It should be noted that a number of other characteristic distortions are also relevant for the structural transformation, though to a lesser extent. The coordinate *q* in Fig. 15g, on the other hand, denotes all other phonon modes that may influence the transition efficiency indirectly, e.g., by periodically modulating the optical absorption of the surface [51].

In summary, the above double-pulse ULEED experiments demonstrate coherent control over the efficiency of the metal–insulator structural phase transition in atomic indium wires on the Si(111) surface. In this, the existence of long-lived vibrational coherence in shear and rotational phonon modes of the (8×2) structure is crucial. Furthermore, the distinct initial phases and the delay-dependent softening or hardening of the frequency-specific contributions to the switching efficiency suggest different roles of shear and rotation motion in the transition. Our results also form a conceptual link between electronic excitation and band structure dynamics measured by trARPES [63–66] and the structural response observed in trRHEED [43,67,68,109], providing unprecedented insights into energy relaxation in a strongly-coupled, quasi-one-dimensional system. Based on the ballistic motion of the order parameter in response to a quasi-instantaneous reshaping of the PES, we further propose a novel and potentially energy-efficient mechanism to control structural phase transitions, which will be discussed below.

6. Exploring the potential energy surface

6.1. *Off-diagonal transition state*

In addition to the coherent vibrational control of the phase transition, multipulse optical excitation also enables us to draw conclusions about the potential energy surface governing the nonequilibrium structural dynamics. Because of the crucial role of the antisymmetric shear and the hexagonal rotation modes in the transition, the natural representation of the PES is given in terms of shear and rotation distortions (see Fig. 16). Previous studies have described the (8×2)→(4×1) transition on a one-dimensional PES. This implies that the structural or reaction coordinate, respectively, represents a straight line between (8×2) and (4×1) configurations on the 2D PES spanned by the two key structural distortions. In this picture, the transition state *T** is located on this line, synonymous with equivalent roles of shear and rotation motion. However, the different characteristics of the two modes observed by ULEED suggest a distinct minimum-energy pathway for the transition, which we discuss in the following.

Whereas both modes leave their signature in the switching efficiency measured by ULEED, the opposing frequency changes around $\Delta t_{p\text{-}p} = 0$, as well as the considerably larger shear amplitude in ULEED compared with the rotation mode are difficult to reconcile with a one-dimensional model. Instead, we continue by a description of the transition in terms of the two-dimensional PES proposed above, which is spanned by the rotation and shear deformations of the (4×1) structure (Fig. 6.12a). Here, the system initially resides in the

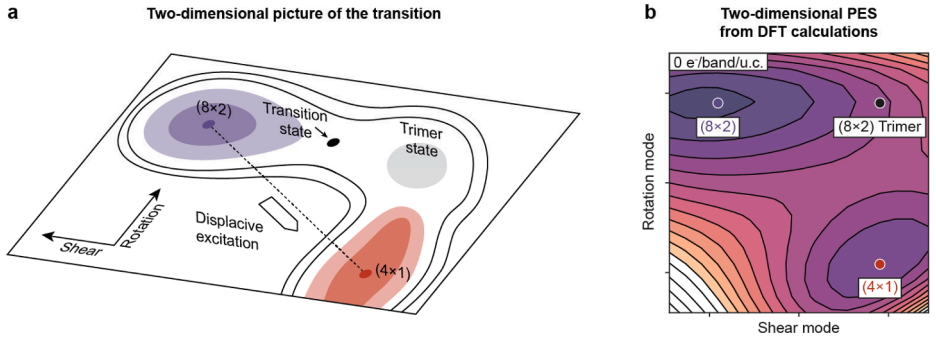

Fig. 16. Two-dimensional picture of the phase transition dynamics. a, Proposed two-dimensional model of the potential energy surface for the (8×2)→(4×1) transition in shear/rotation configuration space, exhibiting a transition state along the shear axis from the (8×2) state (taken from Ref. [51]). b, Two-dimensional ground state PES spanned by shear and trimer (rotation) coordinates from DFT calculations. Taken from Ref. [52]. Black points indicate locations of hexagon, zigzag and trimer structures. White dashed line, direct transition path. Note that the optimum transition path is curved (off-diagonal transition state).

(8×2) minimum (top left) which is separated from the (4×1) state (bottom right) by a finite energy barrier. To understand the generation and the role of coherent atomic motions along shear and rotation coordinates, we consider the effect of ultrafast electronic excitation on the PES. DFT calculations [52] show that the (8×2) minimum of the excited PES is shifted quasi-instantaneously towards the high-symmetry state following optical excitation by the first pump pulse (see dashed black line in Fig. 16a). This in turn leads to a displacive excitation of coherent oscillations in the local (8×2) potential. In this respect, the ULEED measurements evidence that the switching efficiency for the second pulse becomes a strong function of the momentary vibrational state in this intermediate potential.

The combined observations, which include the varying amplitudes of both modes, as well as their distinct phases in the double-pulse traces (Fig. 15), suggest an 'off-diagonal' transition state in configuration space. This state is characterized by a reduced shear but a largely unchanged rotation distortion compared to the (8×2) state (refer to Fig. 16a). This interpretation is further supported by the transient softening of the shear mode and the hardening of the rotation mode near $\Delta t_{p\text{-}p} = 0$ (Fig. 15c and g). Moreover, the two-dimensional ground state PES obtained from DFT calculations clearly exhibits an off-diagonal transition state (Fig. 16b). On this PES, the 'direct' pathway between (8×2) and (4×1) configurations proposed in Ref. [67] does not represent the lowest energy pathway for the transition, since it crosses the barrier at a distance from the transition state for which the activation energy is minimized. Speculating about potential consequences of an off-diagonal transition state, a series of two or more properly timed pump pulses could potentially reach transition efficiencies unattainable by a single excitation. Moreover, depending on the actual location of T^* relative to the direct pathway between (8×2) and (4×1) states, the shear displacement may even be referred to as the primary reaction coordinate, whereas the rotation completing the transition is of a secondary nature. In this case, overcoming an 'early' barrier [54], the indium chains would be first 'un-sheared' and subsequently transformed into the zigzag structure by a rotation. At the same time, the lateral displacement of T^* in Fig. 16b does not support the picture of an early-barrier transition.

Beyond the description of the ground state PES, DFT can be amended to model the evolution of the order parameter in the nonequilibrium (8×2)→(4×1) transition after ultrafast optical excitation. For this purpose, the excited state PES is calculated by manually placing electrons (holes) in conduction (valence) band states coupled to shear and rotation modes or the weakening and strengthening of specific indium-indium bonds [67]. Combined trARPES/DFT studies of the transition showcased how experimental input can advance such model calculations, highlighting the roles of localized photoholes and a broad momentum distribution of

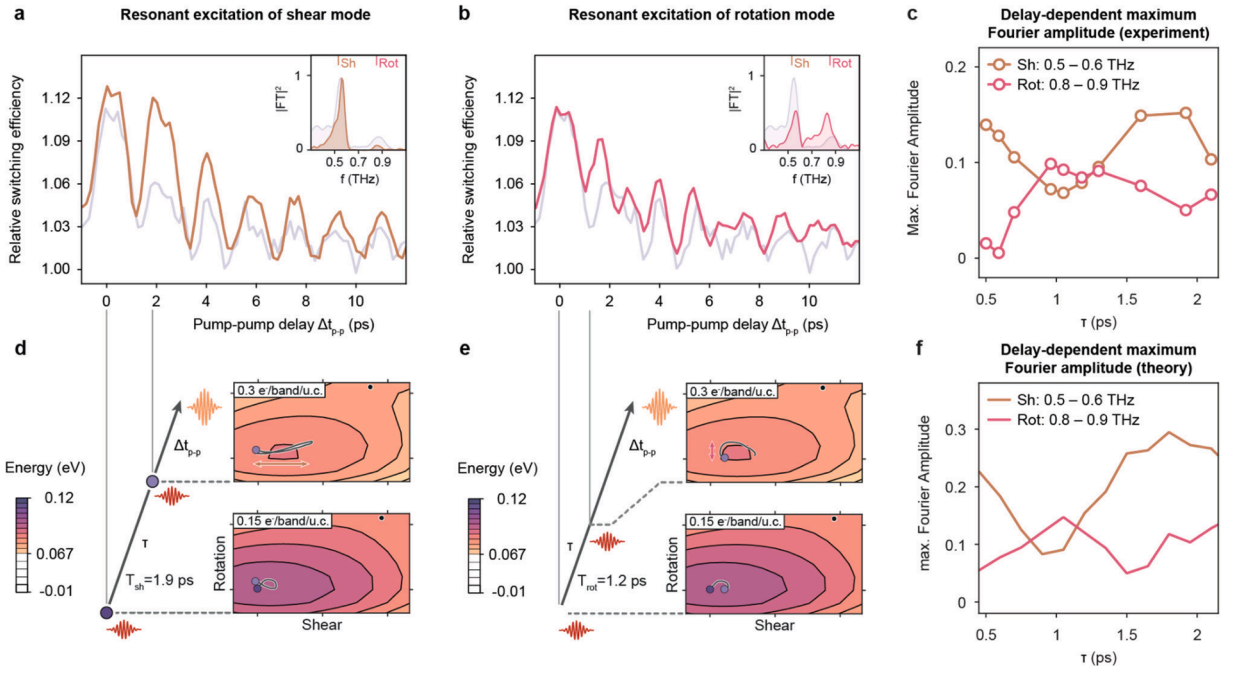

Fig. 17. Mode-selective excitation of the phase transition. a, Selective steering of the ballistic trajectory along the shear mode using timed pulse sequences. Two weak preparation pulses, separated by the delay τ, induce a well-defined vibrational state which is probed by an intense switch pulse after $\Delta t_{p\text{-}p}$. The resulting switching efficiency (orange) directly depends on the momentary nuclear displacements and shows a corresponding modulation of the frequency content, compared to an excitation with a single preparation pulse (light blue). Enhancement and suppression of the shear (0.54 THz) and rotation (0.85 THz) mode, respectively, is depicted in the Fourier transform. b, Analogous steering of the vibrational motion along the rotation mode. c, τ-dependent modulation of shear (0.5–0.6 THz) and rotation (0.8–0.9 THz) mode amplitudes after Fourier transformation along $\Delta t_{p\text{-}p}$. d, Ab-initio DFT, combined with molecular dynamics calculations show the initiated nuclear motion toward the (4×1) structure, following an electronic excitation via displacive excitation of coherent phonons in the underlying 2D PES. The described trajectory is directed along the shear coordinate by timing a second pulse to the shear mode oscillation period ($\tau = T_{sh}$). A third switch pulse is used to strongly deform the 2D PES and overcome the transition barrier (delay time $\Delta t_{p\text{-}p}$). e, Analogous steering along the rotation mode ($\tau = T_{rot}$). f, τ-dependent mode amplitudes, extracted from coarse-grained MD simulations. Taken from Ref. [52]. (For interpretation of the references to color in this figure legend, the reader is referred to the web version of this article.)

excited electrons [63]. This raises the question of what information about the PES and possible transition pathways can be inferred from ULEED. We therefore continue by discussing the combination of ULEED experiments aimed at the selective excitation of shear and rotation modes with DFT calculations and *ab-initio* molecular dynamics (AIMD) simulations.

6.2. Mode-selective excitation

The demonstrated coherent control of the phase transition efficiency via optical pulses implies a substantial contribution of nuclear kinetic energy for overcoming the energy barrier within the two-dimensional PES. Moreover, the results suggest that active manipulation of the transition pathway can be accomplished by carefully timing subthreshold excitation sequences to the vibrational periods of shear and rotation modes (Fig. 17). Specifically, by tuning the delay between two weaker pulses to either amplify or suppress the mode amplitude, the vibrational motion is selectively controlled. A subsequent, more intense switch pulse reveals the induced dynamics via its impact on the transition efficiency. In this scenario, an initial displacive deformation of the PES towards the (4×1) structure triggers coherent nuclear motion along both modes within the (8×2) potential well (Fig. 17d,e). The following optical excitation initiates additional impulsive motion, which interferes with the first and finally impacts directly on the probability to overcome the transition barrier after the switch pulse excitation.

Fig. 17 displays combined theoretical and experimental results on the vibrational response for a system, specifically manipulated by preparing it with a pulse pair, separated by a delay τ, and probing it via the switching efficiency as function of the switch pulse timing $\Delta t_{p\text{-}p}$. When the individual phonons are resonantly driven, the measured traces show enhanced oscillations from either the shear (Fig. 17a) or the rotation (Fig. 17b) mode, as quantified by the respective Fourier transform (inset). Furthermore, the shear mode and, to a much lesser extent, the rotation mode peaks show a distinct low-frequency tail, which is attributed to time-dependent electronic softening and anharmonicity of the excited potential, as the system is driven close to the transition threshold. A systematic measurement of the phonon amplitudes as a function of inter-pulse delay τ demonstrates the selectivity of the employed control scheme (Fig. 17 (c)). Exclusive shear motion is achieved for out-of-phase excitation with the rotation mode at $\tau = 0.6$ ps. The opposite case at $\tau = 1$ ps, however, leaves a remaining shear mode amplitude and thus yields an incomplete cancellation.

DFT and AIMD calculations complement the above experimental findings and illustrate the amplitude enhancement from in-phase excitation with the shear (Fig. 17d) and rotation mode (Fig. 17e). The numerical treatment follows previous studies [67,120] by incorporating the population and depopulation of zone-center and zone-boundary states, respectively, leading to the displacive distortion of the potential towards the (4×1) structure. While keeping the electronic occupation constant, the resulting nuclear motion in response to the sudden deformation is mapped onto the displacements along the shear and rotation transformation vectors. Apart from the depicted exemplary AIMD trajectories at $T = 0$ K, statistical sampling at experimental conditions ($T = 60$ K) was performed with coarse-grained molecular dynamics. The exact location of the off-diagonal transition state yields characteristic timing-dependent phonon amplitudes, imprinted in the switching efficiency, in excellent qualitative agreement with experimental results (Fig. 17e). The combined experimental and theoretical approach thus clearly shows the selective steering of amplitude mode motion along a Peierls transition and demonstrates the role of kinetic energy for overcoming energy barriers.

7. Summary and outlook

This review summarizes the contributions of ULEED and OPP to the understanding of In/Si(111), most importantly, the ultrafast probing and coherent vibrational control of the (8×2)→(4×1) phase transition [51,52]. Our findings demonstrate, among others, the coherent control over a metal–insulator structural phase transition by manipulating the amplitudes of key phonon modes connecting both phases. More specifically, by combining ultrafast low-energy electron diffraction (ULEED) with timed sequences of femtosecond light pulses, we have explored the control of the Peierls transition in indium wires on silicon, enabled by coherent shear and rotation phonons. The results confirm the applicability of coherent control concepts from femtochemistry to solids and create strong conceptual links between the two fields. The key findings concerning nonequilibrium structural dynamics are summarized below:

1) *Coherent atomic motion can be harnessed to control the efficiency of structural phase transitions.* By analogy with repeatedly pushing a child on a swing, pulse sequences tuned in resonance with decisive lattice modes can amplify the vibrational amplitude along selected trajectories on a transiently excited PES, e.g., over a barrier and towards metastable or hidden states. Moreover, provided a sufficiently strong coupling of the relevant phonon modes to specific electronic excitations, such transitions can be driven far from equilibrium, i.e., well below the critical temperature predicted by thermodynamics. Mode-selective excitation can be achieved by three-pulse excitation schemes featuring two weak preparation pulses (separated by the desired phonon period) and a stronger switching pulse. These schemes significantly enhance the degree of control over materials, controlling physical and chemical functionality on ultrafast timescales. The applicability of coherent vibrational control to other classes of materials such as 2D materials has been employed by Maklar *et al.* [53] in the switching to a metastable metallic state of 1*T*-TaS_2.
2) *Kinetic energy stored in the coherent motion of the nuclei contributes to overcoming the transition state.* The question of whether and how the inertial motion of atoms during a phase transition can contribute to overcoming energy barriers is as old as the field of femtochemistry itself. Together with the seminal work of T. Frigge *et al.* [67], and in combination with density functional theory calculations as well as molecular dynamics simulations [52], our results provide strong evidence for the ballistic nature of the order parameter in the (8×2)→(4×1) transition. In some analogy to a roller coaster ride, the In/Si (111) system can thus overcome finite energy barriers, due to the inertial motion of the atoms involved. This suggests that the kinetic energy stored in the nuclear motion during a nonequilibrium phase transition can, in principle, be harnessed to drive phase transitions more energy-efficiently.

3) *In combination with ULEED or other time-resolved diffraction/spectroscopy techniques, multi-pulse optical excitation of solids provides a novel tool to explore the transient potential energy surface (PES) of structural phase transitions*. We have successfully demonstrated that by analyzing the relative amplitudes as well as the delay-dependent frequencies of shear and rotation modes, valuable information about the location of the transition state on the two-dimensional PES of the (8×2)→(4×1) transition can be obtained. Given Polanyi's rules [54], i.e., the effects of transition state location on the role of vibrational excitation during chemical reactions, such information could be key to efficiently controlling solid-state transitions between initial and final states enabled by phonon coherences.
4) Finally, our findings showcase how *microscopic heterogeneity affects nonequilibrium phase transitions*. Concerning the In/Si(111) system, the coexistence of insulating and metallic domains below the critical temperature not only influences the leverage of coherent control schemes, but, naturally, also leads to the formation of dynamic interfaces between both phases, i.e., atomic-scale metal–insulator junctions [48]. In general, the dynamics of domains, domain walls and different types of defects in low-dimensional and correlated materials heavily influence the macroscopic properties and functionalities of the latter and thus deserve further consideration. While ULEED can only indirectly measure the impact of microscopic heterogeneity, future time- and spatially-resolved surface probes could observe propagating phase fronts, and finally manipulate phase transitions on femtosecond time and micrometer-to-nanometer length scales.

The In/Si(111) surface has clearly earned its label of being a 'model system'. Almost 60 years after its discovery, this fascinating surface system still holds surprises, as evidenced by studies on its nonequilibrium dynamics. Future studies could exploit the one-dimensional nature of the system and control the efficiency of the Peierls transition via the polarization of the optical excitation or harness the coupling of shear and rotation modes to distinct electronic states in orbital-selective control schemes.

CRediT authorship contribution statement

Jan Gerrit Horstmann: Conceptualization, Methodology, Software, Validation, Formal analysis, Investigation, Writing – original draft, Writing – review & editing, Visualization. **Hannes Böckmann:** Conceptualization, Methodology, Software, Validation, Formal analysis, Investigation, Writing – original draft, Writing – review & editing, Visualization. **Felix Kurtz:** Methodology, Validation, Investigation, Writing – review & editing. **Gero Storeck:** Methodology, Software, Writing – review & editing. **Claus Ropers:** Conceptualization, Validation, Resources, Writing – original draft, Writing – review & editing, Supervision, Project administration, Funding acquisition.

Declaration of competing interest

The authors declare that they have no known competing financial interests or personal relationships that could have appeared to influence the work reported in this paper.

Acknowledgments

This work was supported by the EUROPEAN RESEARCH COUNCIL [ERC Starting Grant 'ULEED', ID: 639119; ERC Advanced Grant 'ULEEM', 101055435]; the Deutsche Forschungsgemeinschaft [SFB-1073, project A05] and an ETH Zurich Postdoctoral Fellowship [ETH fellow: J.G.H.]. We acknowledge insightful discussions with Stefan Wippermann, Martin Wolf, Ralph Ernstorfer, and Michael Horn-von Hoegen.

References

[1] J. Bardeen, L.N. Cooper, J.R. Schrieffer, Theory of superconductivity, Phys. Rev. 108 (1957) 1175–1204, https://doi.org/10.1103/PhysRev.108.1175.
[2] J.G. Bednorz, K.A. Müller, Possible high T_c superconductivity in the Ba−La−Cu−O system, Z. Für Phys. B Condens. Matter 64 (1986) 189–193, https://doi.org/10.1007/BF01303701.
[3] Y. Cao, V. Fatemi, S. Fang, K. Watanabe, T. Taniguchi, E. Kaxiras, P. Jarillo-Herrero, Unconventional superconductivity in magic-angle graphene superlattices, Nature 556 (2018) 43–50, https://doi.org/10.1038/nature26160.
[4] N.F. Mott, Metal-insulator transitions, second ed., Taylor & Trancis Ltd., London New York Philadelphia, 1990.
[5] Y. Cao, V. Fatemi, A. Demir, S. Fang, S.L. Tomarken, J.Y. Luo, J.D. Sanchez-Yamagishi, K. Watanabe, T. Taniguchi, E. Kaxiras, R.C. Ashoori, P. Jarillo-Herrero, Correlated insulator behaviour at half-filling in magic-angle graphene superlattices, Nature 556 (2018) 80–84, https://doi.org/10.1038/nature26154.
[6] C.N. Lau, F. Xia, L. Cao, Emergent quantum materials, MRS Bull. 45 (2020) 340–347, https://doi.org/10.1557/mrs.2020.125.
[7] T. Giamarchi, Quantum Physics in One Dimension, Clarendon Press, Oxford, 2004. https://oxford.universitypressscholarship.com/view/10.1093/acprof:oso/9780198525004.001.0001/acprof-9780198525004 (accessed November 18, 2020).
[8] R.E. Peierls, Quantum theory of solids, Clarendon Press, Oxford, 1955.
[9] C. Blumenstein, J. Schäfer, S. Mietke, S. Meyer, A. Dollinger, M. Lochner, X.Y. Cui, L. Patthey, R. Matzdorf, R. Claessen, Atomically controlled quantum chains hosting a tomonaga-luttinger liquid, Nat. Phys. 7 (2011) 776–780, https://doi.org/10.1038/nphys2051.
[10] G. Grüner, Density waves in solids, 1st ed., CRC Press, Boca Raton, 1994.
[11] G. Grüner, The dynamics of charge-density waves, Rev. Mod. Phys. 60 (1988) 1129–1181, https://doi.org/10.1103/RevModPhys.60.1129.
[12] W.A. Little, Possibility of synthesizing an organic superconductor, Phys. Rev. 134 (1964) A1416–A1424, https://doi.org/10.1103/PhysRev.134.A1416.
[13] F. Herbert, On the theory of superconductivity: the one-dimensional case, Proc. R. Soc. Lond. Ser. Math. Phys. Sci. 223 (1954) 296–305, https://doi.org/10.1098/rspa.1954.0116.
[14] A. Overhauser, Anomalous effects in simple metals, Wiley VCH Verlag GmbH & Co. KGaA, Weinheim, 2010.
[15] K. Rossnagel, On the origin of charge-density waves in select layered transition-metal dichalcogenides, J. Phys. Condens. Matter 23 (2011) 213001, https://doi.org/10.1088/0953-8984/23/21/213001.

[16] J.A. Wilson, F.J. Di Salvo, S. Mahajan, Charge-density waves in metallic, layered, transition-metal dichalcogenides, Phys. Rev. Lett. 32 (1974) 882–885, https://doi.org/10.1103/PhysRevLett.32.882.

[17] S. Ravy, H. Requardt, D. Le Bolloc'h, P. Foury-Leylekian, J.-P. Pouget, R. Currat, P. Monceau, M. Krisch, Inelastic x-ray scattering study of charge-density-wave dynamics in the $Rb_{0.3}MoO_3$ blue bronze, Phys. Rev. B 69 (2004) 115113, https://doi.org/10.1103/PhysRevB.69.115113.

[18] J.P. Pouget, B. Hennion, C. Escribe-Filippini, M. Sato, Neutron-scattering investigations of the Kohn anomaly and of the phase and amplitude charge-density-wave excitations of the blue bronze $K_{0.3}MoO_3$, Phys. Rev. B 43 (1991) 8421–8430, https://doi.org/10.1103/PhysRevB.43.8421.

[19] G.-H. Gweon, J.D. Denlinger, J.A. Clack, J.W. Allen, C.G. Olson, E. DiMasi, M.C. Aronson, B. Foran, S. Lee, Direct observation of complete Fermi Surface, imperfect nesting, and gap Anisotropy in the high-temperature incommensurate Charge-density-wave compound $SmTe_3$, Phys. Rev. Lett. 81 (1998) 886–889, https://doi.org/10.1103/PhysRevLett.81.886.

[20] J. Laverock, S.B. Dugdale, Zs. Major, M.A. Alam, N. Ru, I.R. Fisher, G. Santi, E. Bruno, Fermi surface nesting and charge-density wave formation in rare-earth tritellurides, Phys. Rev. B 71 (2005), https://doi.org/10.1103/PhysRevB.71.085114.

[21] V. Brouet, W.L. Yang, X.J. Zhou, Z. Hussain, R.G. Moore, R. He, D.H. Lu, Z.X. Shen, J. Laverock, S.B. Dugdale, N. Ru, I.R. Fisher, Angle-resolved photoemission study of the evolution of band structure and charge density wave properties in RTe_3 (R=Y, La, Ce, Sm, Gd, Tb, and Dy), Phys. Rev. B 77 (2008) 235104, https://doi.org/10.1103/PhysRevB.77.235104.

[22] D. Jérome, Organic conductors: from Charge density wave TTF–TCNQ to superconducting (TMTSF)2PF6, Chem. Rev. 104 (2004) 5565–5592, https://doi.org/10.1021/cr030652g.

[23] M. Maiuri, M. Garavelli, G. Cerullo, Ultrafast spectroscopy: state of the art and open challenges, J. Am. Chem. Soc. 142 (2020) 3–15, https://doi.org/10.1021/jacs.9b10533.

[24] J. Lloyd-Hughes, P.M. Oppeneer, T.P. dos Santos, A. Schleife, S. Meng, M.A. Sentef, M. Ruggenthaler, A. Rubio, I. Radu, M. Murnane, X. Shi, H. Kapteyn, B. Stadtmüller, K.M. Dani, F.H. da Jornada, E. Prinz, M. Aeschlimann, R.L. Milot, M. Burdanova, J. Boland, T. Cocker, F. Hegmann, The 2021 ultrafast spectroscopic probes of condensed matter roadmap, J. Phys. Condens. Matter 33 (2021) 353001, https://doi.org/10.1088/1361-648X/abfe21.

[25] M. Bargheer, N. Zhavoronkov, M. Woerner, T. Elsaesser, Recent Progress in ultrafast X-ray Diffraction, ChemPhysChem 7 (2006) 783–792, https://doi.org/10.1002/cphc.200500591.

[26] R. Schoenlein, T. Elsaesser, K. Holldack, Z. Huang, H. Kapteyn, M. Murnane, M. Woerner, Recent advances in ultrafast X-ray sources, Philos. Trans. R. Soc. Math. Phys Eng. Sci. 377 (2019) 20180384, https://doi.org/10.1098/rsta.2018.0384.

[27] D. Filippetto, P. Musumeci, R.K. Li, B.J. Siwick, M.R. Otto, M. Centurion, J.P.F. Nunes, Ultrafast electron diffraction: visualizing dynamic states of matter, Rev. Mod. Phys. 94 (2022) 045004, https://doi.org/10.1103/RevModPhys.94.045004.

[28] A. Feist, G. Storeck, S. Schäfer, C. Ropers, Structural dynamics probed by high-coherence electron pulses, MRS Bull. 43 (2018) 504–511, https://doi.org/10.1557/mrs.2018.153.

[29] A.S. Johnson, D. Perez-Salinas, K.M. Siddiqui, S. Kim, S. Choi, K. Volckaert, P.E. Majchrzak, S. Ulstrup, N. Agarwal, K. Hallman, R.F. Haglund, C.M. Günther, B. Pfau, S. Eisebitt, D. Backes, F. Maccherozzi, A. Fitzpatrick, S.S. Dhesi, P. Gargiani, M. Valvidares, N. Artrith, F. de Groot, H. Choi, D. Jang, A. Katoch, S. Kwon, S.H. Park, H. Kim, S.E. Wall, Ultrafast X-ray imaging of the light-induced phase transition in VO_2, Nat. Phys. 19 (2023) 215–220, https://doi.org/10.1038/s41567-022-01848-w.

[30] A. Ashoka, S. Nagane, N. Strkalj, A. Sharma, B. Roose, A.J. Sneyd, J. Sung, J.L. MacManus-Driscoll, S.D. Stranks, S. Feldmann, A. Rao, Local symmetry breaking drives picosecond spin domain formation in polycrystalline halide perovskite films, Nat. Mater. 22 (2023) 977–984, https://doi.org/10.1038/s41563-023-01550-z.

[31] T. Danz, T. Domröse, C. Ropers, Ultrafast nanoimaging of the order parameter in a structural phase transition, Science 371 (2021) 371–374, https://doi.org/10.1126/science.abd2774.

[32] K. Sokolowski-Tinten, C. Blome, J. Blums, A. Cavalleri, C. Dietrich, A. Tarasevitch, I. Uschmann, E. Förster, M. Kammler, M. Horn-von-Hoegen, D. von der Linde, Femtosecond X-ray measurement of coherent lattice vibrations near the Lindemann stability limit, Nature 422 (2003) 287–289, https://doi.org/10.1038/nature01490.

[33] A. Cavalleri, C.W. Siders, F.L.H. Brown, D.M. Leitner, C. Tóth, J.A. Squier, C.P.J. Barty, K.R. Wilson, K. Sokolowski-Tinten, M. Horn von Hoegen, D. von der Linde, M. Kammler, Anharmonic lattice dynamics in germanium measured with ultrafast X-ray diffraction, Phys. Rev. Lett. 85 (2000) 586–589, https://doi.org/10.1103/PhysRevLett.85.586.

[34] M. Eichberger, H. Schäfer, M. Krumova, M. Beyer, J. Demsar, H. Berger, G. Moriena, G. Sciaini, R.J.D. Miller, Snapshots of cooperative atomic motions in the optical suppression of charge density waves, Nature 468 (2010) 799–802, https://doi.org/10.1038/nature09539.

[35] U. Bovensiepen, P.S. Kirchmann, Elementary relaxation processes investigated by femtosecond photoelectron spectroscopy of two-dimensional materials, Laser Photonics Rev. 6 (2012) 589–606, https://doi.org/10.1002/lpor.201000035.

[36] S. Hellmann, T. Rohwer, M. Kalläne, K. Hanff, C. Sohrt, A. Stange, A. Carr, M.M. Murnane, H.C. Kapteyn, L. Kipp, M. Bauer, K. Rossnagel, Time-domain classification of charge-density-wave insulators, Nat. Commun. 3 (2012) 1069, https://doi.org/10.1038/ncomms2078.

[37] M. Zonno, F. Boschini, A. Damascelli, Time-resolved ARPES on cuprates: Tracking the low-energy electrodynamics in the time domain, J. Electron Spectrosc. Relat. Phenom. 251 (2021) 147091, https://doi.org/10.1016/j.elspec.2021.147091.

[38] D. Afanasiev, J.R. Hortensius, B.A. Ivanov, A. Sasani, E. Bousquet, Y.M. Blanter, R.V. Mikhaylovskiy, A.V. Kimel, A.D. Caviglia, Ultrafast control of magnetic interactions via light-driven phonons, Nat. Mater. 20 (2021) 607–611, https://doi.org/10.1038/s41563-021-00922-7.

[39] P. Němec, M. Fiebig, T. Kampfrath, A.V. Kimel, Antiferromagnetic opto-spintronics, Nat. Phys. 14 (2018) 229–241, https://doi.org/10.1038/s41567-018-0051-x.

[40] E. Beaurepaire, J.-C. Merle, A. Daunois, J.-Y. Bigot, Ultrafast spin dynamics in ferromagnetic nickel, Phys. Rev. Lett. 76 (1996) 4250–4253, https://doi.org/10.1103/PhysRevLett.76.4250.

[41] K. Haupt, M. Eichberger, N. Erasmus, A. Rohwer, J. Demsar, K. Rossnagel, H. Schwoerer, Ultrafast metamorphosis of a complex charge-density wave, Phys. Rev. Lett. 116 (2016) 016402, https://doi.org/10.1103/PhysRevLett.116.016402.

[42] L. Stojchevska, I. Vaskivskyi, T. Mertelj, P. Kusar, D. Svetin, S. Brazovskii, D. Mihailovic, Ultrafast switching to a stable hidden quantum state in an electronic crystal, Science 344 (2014) 177–180, https://doi.org/10.1126/science.1241591.

[43] S. Wall, B. Krenzer, S. Wippermann, S. Sanna, F. Klasing, A. Hanisch-Blicharski, M. Kammler, W.G. Schmidt, M. Horn-von Hoegen, Atomistic picture of charge density wave formation at surfaces, Phys. Rev. Lett. 109 (2012) 186101, https://doi.org/10.1103/PhysRevLett.109.186101.

[44] E.J. Sie, C.M. Nyby, C.D. Pemmaraju, S.J. Park, X. Shen, J. Yang, M.C. Hoffmann, B.K. Ofori-Okai, R. Li, A.H. Reid, S. Weathersby, E. Mannebach, N. Finney, D. Rhodes, D. Chenet, A. Antony, L. Balicas, J. Hone, T.P. Devereaux, T.F. Heinz, X. Wang, A.M. Lindenberg, An ultrafast symmetry switch in a Weyl semimetal, Nature 565 (2019) 61, https://doi.org/10.1038/s41586-018-0809-4.

[45] N.D. Mermin, H. Wagner, Absence of ferromagnetism or antiferromagnetism in one- or two-dimensional isotropic Heisenberg models, Phys. Rev. Lett. 17 (1966) 1133–1136, https://doi.org/10.1103/PhysRevLett.17.1133.

[46] B. Hafke, C. Brand, T. Witte, B. Sothmann, M. Horn-von Hoegen, S.C. Erwin, Thermally induced crossover from 2D to 1D behavior in an Array of atomic wires: silicon dangling-bond solitons in Si(553)-AU, Phys. Rev. Lett. 124 (2020) 016102, https://doi.org/10.1103/PhysRevLett.124.016102.

[47] H. Alloul, J. Bobroff, M. Gabay, P.J. Hirschfeld, Defects in correlated metals and superconductors, Rev. Mod. Phys. 81 (2009) 45–108, https://doi.org/10.1103/RevModPhys.81.45.

[48] S.K. Song, A. Samad, S. Wippermann, H.W. Yeom, Dynamical metal to Charge-density-wave junctions in an atomic wire Array, Nano Lett. 19 (2019) 5769–5773, https://doi.org/10.1021/acs.nanolett.9b02438.

[49] J. Demsar, K. Biljaković, D. Mihailovic, Single Particle and collective excitations in the one-dimensional Charge density wave solid $K_{0.3}MoO_3$ probed in real time by Femtosecond spectroscopy, Phys. Rev. Lett. 83 (1999) 800–803, https://doi.org/10.1103/PhysRevLett.83.800.

[50] H.J. Zeiger, J. Vidal, T.K. Cheng, E.P. Ippen, G. Dresselhaus, M.S. Dresselhaus, Theory for displacive excitation of coherent phonons, Phys. Rev. B 45 (1992) 768–778, https://doi.org/10.1103/PhysRevB.45.768.

[51] J.G. Horstmann, H. Böckmann, B. Wit, F. Kurtz, G. Storeck, C. Ropers, Coherent control of a surface structural phase transition, Nature 583 (2020) 232–236, https://doi.org/10.1038/s41586-020-2440-4.

[52] H. Böckmann, J.G. Horstmann, A.S. Razzaq, S. Wippermann, C. Ropers, Mode-selective ballistic pathway to a metastable electronic phase, Struct. Dyn. 9 (2022) 045102, https://doi.org/10.1063/4.0000162.

[53] J. Maklar, S. Dong, J. Sarkar, Y.A. Gerasimenko, T. Pincelli, S. Beaulieu, P.S. Kirchmann, J.A. Sobota, S.-L. Yang, D. Leuenberger, R.G. Moore, Z.-X. Shen, M. Wolf, D. Mihailovic, R. Ernstorfer, L. Rettig, Coherent Light Control of a Metastable Hidden Phase (2022). https://doi.org/10.48550/arXiv.2206.03788.

[54] J.C. Polanyi, W.H. Wong, Location of energy barriers. I. effect on the dynamics of reactions A + BC, J. Chem. Phys. 51 (1969) 1439–1450, https://doi.org/10.1063/1.1672194.

[55] H.W. Yeom, S. Takeda, E. Rotenberg, I. Matsuda, K. Horikoshi, J. Schaefer, C.M. Lee, S.D. Kevan, T. Ohta, T. Nagao, S. Hasegawa, Instability and charge density wave of metallic quantum chains on a silicon surface, Phys. Rev. Lett. 82 (1999) 4898–4901, https://doi.org/10.1103/PhysRevLett.82.4898.

[56] P.C. Snijders, H.H. Weitering, Colloquium: electronic instabilities in self-assembled atom wires, Rev. Mod. Phys. 82 (2010) 307–329, https://doi.org/10.1103/RevModPhys.82.307.

[57] J.R. Ahn, J.H. Byun, H. Koh, E. Rotenberg, S.D. Kevan, H.W. Yeom, Mechanism of gap opening in a triple-band peierls system. in atomic wires on si, Phys. Rev. Lett. 93 (2004) 106401, https://doi.org/10.1103/PhysRevLett.93.106401.

[58] C. Kumpf, O. Bunk, J.H. Zeysing, Y. Su, M. Nielsen, R.L. Johnson, R. Feidenhans'l, K. Bechgaard, Low-temperature structure of indium quantum chains on silicon, Phys. Rev. Lett. 85 (2000) 4916–4919, https://doi.org/10.1103/PhysRevLett.85.4916.

[59] F. Klasing, T. Frigge, B. Hafke, B. Krenzer, S. Wall, A. Hanisch-Blicharski, M. Horn-von Hoegen, Hysteresis proves that the In/Si(111) (8x2) to (4x1) phase transition is first-order, Phys. Rev. B 89 (2014) 121107, https://doi.org/10.1103/PhysRevB.89.121107.

[60] G. Lee, J. Guo, E.W. Plummer, Real-space observation of nanoscale inhomogeneities and fluctuations in a phase transition of a Surface quasi-one-dimensional system: In/Si(111), Phys. Rev. Lett. 95 (2005) 116103, https://doi.org/10.1103/PhysRevLett.95.116103.

[61] S.J. Park, H.W. Yeom, J.R. Ahn, I.-W. Lyo, Atomic-scale phase coexistence and fluctuation at the quasi-one-dimensional metal-insulator transition, Phys. Rev. Lett. 95 (2005) 126102, https://doi.org/10.1103/PhysRevLett.95.126102.

[62] Y.J. Sun, S. Agario, S. Souma, K. Sugawara, Y. Tago, T. Sato, T. Takahashi, Cooperative structural and peierls transition of indium chains on Si(111), Phys. Rev. B 77 (2008) 125115, https://doi.org/10.1103/PhysRevB.77.125115.

[63] C.W. Nicholson, A. Lücke, W.G. Schmidt, M. Puppin, L. Rettig, R. Ernstorfer, M. Wolf, Beyond the molecular movie: dynamics of bands and bonds during a photoinduced phase transition, Science 362 (2018) 821–825, https://doi.org/10.1126/science.aar4183.

[64] C.W. Nicholson, M. Puppin, A. Lücke, U. Gerstmann, M. Krenz, W.G. Schmidt, L. Rettig, R. Ernstorfer, M. Wolf, Excited-state band mapping and momentum-resolved ultrafast population dynamics in In/Si(111) nanowires investigated with XUV-based time- and angle-resolved photoemission spectroscopy, Phys. Rev. B 99 (2019) 155107, https://doi.org/10.1103/PhysRevB.99.155107.

[65] M. Chávez-Cervantes, R. Krause, S. Aeschlimann, I. Gierz, Band structure dynamics in indium wires, Phys. Rev. B 97 (2018) 201401, https://doi.org/10.1103/PhysRevB.97.201401.

[66] M. Chávez-Cervantes, G.E. Topp, S. Aeschlimann, R. Krause, S.A. Sato, M.A. Sentef, I. Gierz, Charge density wave melting in one-dimensional wires with Femtosecond subgap excitation, Phys. Rev. Lett. 123 (2019) 036405, https://doi.org/10.1103/PhysRevLett.123.036405.

[67] T. Frigge, B. Hafke, T. Witte, B. Krenzer, C. Streubühr, A. Samad Syed, V. Mikšić Trontl, I. Avigo, P. Zhou, M. Ligges, D. von der Linde, U. Bovensiepen, M. Horn-von Hoegen, S. Wippermann, A. Lücke, S. Sanna, U. Gerstmann, W.G. Schmidt, Optically excited structural transition in atomic wires on surfaces at the quantum limit, Nature 544 (2017) 207–211, https://doi.org/10.1038/nature21432.

[68] B. Hafke, T. Witte, D. Janoschka, P. Dreher, F.-J. Meyer zu Heringdorf, M. Horn-von Hoegen, Condensation of ground state from a supercooled phase in the Si (111)-(4 x1)->(8x2)-indium atomic wire system, Struct. Dyn. 6 (2019) 045101, https://doi.org/10.1063/1.5111636.

[69] W. Bludau, A. Onton, W. Heinke, Temperature dependence of the band gap of silicon, J. Appl. Phys. 45 (1974) 1846–1848, https://doi.org/10.1063/1.1663501.

[70] J.J. Lander, J. Morrison, Surface reactions of silicon (111) with aluminum and indium, J. Appl. Phys. 36 (1965) 1706–1713, https://doi.org/10.1063/1.1703113.

[71] E. Ganz, H. Ing-Shouh, X. Fulin, S.K. Theiss, J. Golovchenko, Growth and morphology of Pb on Si(111), Surf. Sci. 257 (1991) 259–273, https://doi.org/10.1016/0039-6028(91)90797-V.

[72] G. Le Lay, The Au/Si(111) interface: growth mode, energetics, structural and electronic properties, J. Cryst. Growth 54 (1981) 551–557, https://doi.org/10.1016/0022-0248(81)90512-1.

[73] A.A. Baski, J. Nogami, C.F. Quate, Si(111)-5x1-Au reconstruction as studied by scanning tunneling microscopy, Phys. Rev. B 41 (1990) 10247–10249, https://doi.org/10.1103/PhysRevB.41.10247.

[74] C. Tegenkamp, T. Ohta, J.L. McChesney, H. Dil, E. Rotenberg, H. Pfnür, K. Horn, Coupled Pb chains on Si(557): origin of one-dimensional conductance, Phys. Rev. Lett. 100 (2008) 076802, https://doi.org/10.1103/PhysRevLett.100.076802.

[75] T. Abukawa, M. Sasaki, F. Hisamatsu, T. Goto, T. Kinoshita, A. Kakizaki, S. Kono, Surface electronic structure of a single-domain Si(111)4x1-in surface: a synchrotron radiation photoemission study, Surf. Sci. 325 (1995) 33–44, https://doi.org/10.1016/0039-6028(94)00693-8.

[76] E. Rotenberg, H. Koh, K. Rossnagel, H.W. Yeom, J. Schäfer, B. Krenzer, M.P. Rocha, S.D. Kevan, Indium $\sqrt{7}x\sqrt{3}$ on Si(111): a Nearly free electron metal in two dimensions, Phys. Rev. Lett. 91 (2003) 246404, https://doi.org/10.1103/PhysRevLett.91.246404.

[77] B. Hafke, T. Frigge, T. Witte, B. Krenzer, J. Aulbach, J. Schäfer, R. Claessen, S.C. Erwin, M. Horn-von hoegen, Two-dimensional interaction of spin chains in the Si(553)-Au nanowire system, Phys. Rev. B 94 (2016) 161403, https://doi.org/10.1103/PhysRevB.94.161403.

[78] J.A. Lipton-Duffin, A.G. Mark, J.M. MacLeod, A.B. McLean, Si(557)-Ag: a metallic quasi-one-dimensional system, Phys. Rev. B 77 (2008) 125419, https://doi.org/10.1103/PhysRevB.77.125419.

[79] M. Jäger, H. Pfnür, M. Fanciulli, A.P. Weber, J.H. Dil, C. Tegenkamp, Formation of Sn-induced nanowires on Si(557), Phys. Status Solidi B 256 (2019) 1970037, https://doi.org/10.1002/pssb.201970037.

[80] M. Kawaji, S. Baba, A. Kinbara, Superstructures of submonolayer indium films on silicon (111)7 surfaces, Appl. Phys. Lett. 34 (1979) 748–749, https://doi.org/10.1063/1.90659.

[81] S. Baba, H. Hirayama, J.M. Zhou, A. Kinbara, Adatoms of indium on Si(111) surfaces: application of reflection high energy electron diffraction to desorption experiments, Thin Solid Films 90 (1982) 57–61, https://doi.org/10.1016/0040-6090(82)90071-2.

[82] S. Wippermann, Understanding substrate-supported atomic-scale nanowires from ab initio theory, Universität Paderborn, 2010. https://digital.ub.uni-paderborn.de/hsmig/content/titleinfo/1631 (accessed July 13, 2020).

[83] S.V. Ryjkov, T. Nagao, V.G. Lifshits, S. Hasegawa, Phase transition and stability of Si(111)–8x'2'-in surface phase at low temperatures, Surf. Sci. 488 (2001) 15–22, https://doi.org/10.1016/S0039-6028(01)01145-1.

[84] T. Tanikawa, I. Matsuda, T. Kanagawa, S. Hasegawa, Surface-state electrical conductivity at a metal-insulator transition on silicon, Phys. Rev. Lett. 93 (2004) 016801, https://doi.org/10.1103/PhysRevLett.93.016801.

[85] S. Wippermann, W.G. Schmidt, Entropy explains metal-insulator transition of the Si(111)-in nanowire array, Phys. Rev. Lett. 105 (2010) 126102, https://doi.org/10.1103/PhysRevLett.105.126102.

[86] E. Jeckelmann, S. Sanna, W.G. Schmidt, E. Speiser, N. Esser, Grand canonical peierls transition in In/Si(111), Phys. Rev. B 93 (2016) 241407, https://doi.org/10.1103/PhysRevB.93.241407.

[87] S. Hatta, Y. Ohtsubo, T. Aruga, S. Miyamoto, H. Okuyama, H. Tajiri, O. Sakata, Dynamical fluctuations in in nanowires on Si(111), Phys. Rev. B 84 (2011) 245321, https://doi.org/10.1103/PhysRevB.84.245321.

[88] S. Cheon, T.-H. Kim, S.-H. Lee, H.W. Yeom, Chiral solitons in a coupled double peierls chain, Science 350 (2015) 182–185, https://doi.org/10.1126/science.aaa7055.

[89] H. Morikawa, C.C. Hwang, H.W. Yeom, Controlled electron doping into metallic atomic wires: Si(111)4x1-in, Phys. Rev. B 81 (2010) 075401, https://doi.org/10.1103/PhysRevB.81.075401.

[90] H. Shim, Y. Jeon, J. Yeo, G. Lee, Homogeneous and heterogeneous nucleations in the surface phase transition: Si(111)4x1-in, New J. Phys. 17 (2015) 063026, https://doi.org/10.1088/1367-2630/17/6/063026.

[91] S. Mizuno, Y.O. Mizuno, H. Tochihara, Structural determination of indium-induced Si(111) reconstructed surfaces by LEED analysis: (\sqrt3x\sqrt3)R30^\circ and (4x1), Phys. Rev. B 67 (2003) 195410, https://doi.org/10.1103/PhysRevB.67.195410.

[92] N. Nakamura, K. Anno, S. Kono, Structure analysis of the single-domain Si(111)4x1-in surface by μ-probe auger electron diffraction and μ-probe reflection high energy electron diffraction, Surf. Sci. 256 (1991) 129–134, https://doi.org/10.1016/0039-6028(91)91208-F.

[93] Y. Fukaya, M. Hashimoto, A. Kawasuso, A. Ichimiya, Surface structure of Si(111)-(8x2)–In determined by reflection high-energy positron diffraction, Surf. Sci. 602 (2008) 2448–2452, https://doi.org/10.1016/j.susc.2008.05.021.

[94] O. Bunk, G. Falkenberg, J.H. Zeysing, L. Lottermoser, R.L. Johnson, M. Nielsen, F. Berg-Rasmussen, J. Baker, R. Feidenhans'l, Structure determination of the indium-induced Si(111)-(4x1) reconstruction by surface x-ray diffraction, Phys. Rev. B 59 (1999) 12228–12231, https://doi.org/10.1103/PhysRevB.59.12228.

[95] J.R. Ahn, J.H. Byun, J.K. Kim, H.W. Yeom, Absence of dynamic fluctuation in metallic in chains on Si(111): Core-level and valence-band photoemission study, Phys. Rev. B 75 (2007) 033313, https://doi.org/10.1103/PhysRevB.75.033313.

[96] C. Liu, T. Inaoka, S. Yaginuma, T. Nakayama, M. Aono, T. Nagao, Disappearance of the quasi-one-dimensional plasmon at the metal-insulator phase transition of indium atomic wires, Phys. Rev. B 77 (2008) 205415, https://doi.org/10.1103/PhysRevB.77.205415.

[97] F. Pedreschi, J.D. O'Mahony, P. Weightman, J.R. Power, Evidence of electron confinement in the single-domain (4x1)-in superstructure on vicinal Si(111), Appl. Phys. Lett. 73 (1998) 2152–2154, https://doi.org/10.1063/1.122407.

[98] K. Fleischer, S. Chandola, N. Esser, W. Richter, J.F. McGilp, Reflectance Anisotropy Spectroscopy of Si(111)-(4x1)-In, Phys. Status Solidi A 188 (2001) 1411–1416. https://onlinelibrary.wiley.com/doi/abs/10.1002/1521-396X%28200112%29188%3A4%3C1411%3A%3AAID-PSSA1411%3E3.0.CO%3B2-%23.

[99] K. Fleischer, S. Chandola, N. Esser, W. Richter, J.F. McGilp, Phonon and polarized reflectance spectra from Si(111)-(4x1): evidence for a charge-density-wave driven phase transition, Phys. Rev. B 67 (2003) 235318, https://doi.org/10.1103/PhysRevB.67.235318.

[100] K. Fleischer, S. Chandola, N. Esser, W. Richter, J.F. McGilp, W.G. Schmidt, S. Wang, W. Lu, J. Bernholc, Atomic indium nanowires on Si(111): the (4x1)–(8x2) phase transition studied with reflectance anisotropy spectroscopy, Appl. Surf. Sci. 234 (2004) 302–306, https://doi.org/10.1016/j.apsusc.2004.05.114.

[101] E. Speiser, N. Esser, S. Wippermann, W.G. Schmidt, Surface vibrational Raman modes of In:Si(111) (4x1) and (8x2) nanowires, Phys. Rev. B 94 (2016) 075417, https://doi.org/10.1103/PhysRevB.94.075417.

[102] K. Fleischer, S. Chandola, N. Esser, W. Richter, J.F. McGilp, Surface phonons of the Si(111):In-(4x1) and (8x2) phases, Phys. Rev. B 76 (2007) 205406, https://doi.org/10.1103/PhysRevB.76.205406.

[103] J. Kraft, M.G. Ramsey, F.P. Netzer, Surface reconstructions of in on Si(111), Phys. Rev. B 55 (1997) 5384–5393, https://doi.org/10.1103/PhysRevB.55.5384.

[104] J.L. Stevens, M.S. Worthington, I.S.T. Tsong, 4x1 reconstruction of indium deposited on vicinal Si(111) surfaces, Phys. Rev. B 47 (1993) 1453–1459, https://doi.org/10.1103/PhysRevB.47.1453.

[105] T. Uchihashi, U. Ramsperger, Electron conduction through quasi-one-dimensional indium wires on silicon, Appl. Phys. Lett. 80 (2002) 4169–4171, https://doi.org/10.1063/1.1483929.

[106] T.-H. Kim, H.W. Yeom, Topological solitons versus nonsolitonic phase defects in a quasi-one-dimensional Charge-density wave, Phys. Rev. Lett. 109 (2012) 246802, https://doi.org/10.1103/PhysRevLett.109.246802.

[107] F. Bechstedt, A. Krivosheeva, J. Furthmüller, A.A. Stekolnikov, Vibrational properties of the quasi-one-dimensional Si(111)-(4x1) system, Phys. Rev. B 68 (2003) 193406, https://doi.org/10.1103/PhysRevB.68.193406.

[108] W.-H. Liu, Y.-X. Gu, Z. Wang, S.-S. Li, L.-W. Wang, J.-W. Luo, Origin of immediate damping of coherent oscillations in photoinduced Charge-density-wave transition, Phys. Rev. Lett. 130 (2023) 146901, https://doi.org/10.1103/PhysRevLett.130.146901.

[109] T. Frigge, B. Hafke, T. Witte, B. Krenzer, M. Horn-von Hoegen, Non-equilibrium lattice dynamics of one-dimensional in chains on Si(111) upon ultrafast optical excitation, Struct. Dyn. 5 (2018) 025101, https://doi.org/10.1063/1.5016619.

[110] D.M. Cornelison, M.S. Worthington, I.S.T. Tsong, Si(111)-(4x1)In surface reconstruction studied by impact-collision ion-scattering spectrometry, Phys. Rev. B 43 (1991) 4051–4056, https://doi.org/10.1103/PhysRevB.43.4051.

[111] A.A. Saranin, E.A. Khramtsova, K.V. Ignatovich, V.G. Lifshits, T. Numata, O. Kubo, M. Katayama, I. Katayama, K. Oura, Indium-induced Si(111)4x1 silicon substrate atom reconstruction, Phys. Rev. B 55 (1997) 5353–5359, https://doi.org/10.1103/PhysRevB.55.5353.

[112] A.A. Saranin, A.V. Zotov, K.V. Ignatovich, V.G. Lifshits, T. Numata, O. Kubo, H. Tani, M. Katayama, K. Oura, Structural model for the Si(111)-4x1-in reconstruction, Phys. Rev. B 56 (1997) 1017–1020, https://doi.org/10.1103/PhysRevB.56.1017.

[113] Y. Terada, S. Yoshida, A. Okubo, K. Kanazawa, M. Xu, O. Takeuchi, H. Shigekawa, Optical doping: active control of metal−insulator transition in nanowire, Nano Lett. 8 (2008) 3577–3581, https://doi.org/10.1021/nl801350p.

[114] H. Zhang, F. Ming, H.-J. Kim, H. Zhu, Q. Zhang, H.H. Weitering, X. Xiao, C. Zeng, J.-H. Cho, Z. Zhang, Stabilization and manipulation of electronically phase-Separated ground states in defective indium atom wires on silicon, Phys. Rev. Lett. 113 (2014) 196802, https://doi.org/10.1103/PhysRevLett.113.196802.

[115] S.J. Park, H.W. Yeom, S.H. Min, D.H. Park, I.-W. Lyo, Direct evidence of the Charge ordered phase transition of indium nanowires on Si(111), Phys. Rev. Lett. 93 (2004) 106402, https://doi.org/10.1103/PhysRevLett.93.106402.

[116] J.-H. Cho, D.-H. Oh, K.S. Kim, L. Kleinman, Weakly correlated one-dimensional indium chains on Si(111), Phys. Rev. B 64 (2001) 235302, https://doi.org/10.1103/PhysRevB.64.235302.

[117] O. Gallus, T.h. Pillo, M. Hengsberger, P. Segovia, Y. Baer, A system with a complex phase transition: indium chains on Si(111), Eur. Phys. J. B - Condens. Matter Complex Syst. 20 (2001) 313–319, https://doi.org/10.1007/BF01352592.

[118] A.A. Stekolnikov, K. Seino, F. Bechstedt, S. Wippermann, W.G. Schmidt, A. Calzolari, M.B. Nardelli, Hexagon versus Trimer formation in in nanowires on Si (111): energetics and quantum conductance, Phys. Rev. Lett. 98 (2007) 026105, https://doi.org/10.1103/PhysRevLett.98.026105.

[119] C. González, J. Ortega, F. Flores, Metal–insulator transition in one-dimensional in-chains on Si(111): combination of a soft shear distortion and a double-band peierls instability, New J. Phys. 7 (2005) 100–107, https://doi.org/10.1088/1367-2630/7/1/100.

[120] A. Lücke, U. Gerstmann, T.D. Kühne, W.G. Schmidt, Efficient PAW-based bond strength analysis for understanding the In/Si(111)(8x2) – (4x1) phase transition, J. Comput. Chem. 38 (2017) 2276–2282, https://doi.org/10.1002/jcc.24878.

[121] H.-J. Kim, J.-H. Cho, Driving force of phase transition in indium nanowires on Si(111), Phys. Rev. Lett. 110 (2013) 116801, https://doi.org/10.1103/PhysRevLett.110.116801.

[122] S.-W. Kim, J.-H. Cho, Origin of the metal-insulator transition of indium atom wires on Si(111), Phys. Rev. B 93 (2016) 241408, https://doi.org/10.1103/PhysRevB.93.241408.

[123] W.G. Schmidt, S. Wippermann, S. Sanna, M. Babilon, N.J. Vollmers, U. Gerstmann, In-Si(111)(4x1)/(8x2) nanowires: electron transport, entropy, and metal-insulator transition, Phys. Status Solidi B 249 (2012) 343–359, https://doi.org/10.1002/pssb.201100457.

[124] C. González, F. Flores, J. Ortega, Soft phonon, dynamical fluctuations, and a reversible phase transition: indium chains on silicon, Phys. Rev. Lett. 96 (2006) 136101, https://doi.org/10.1103/PhysRevLett.96.136101.

[125] C. González, J. Guo, J. Ortega, F. Flores, H.H. Weitering, Mechanism of the band gap opening across the order-Disorder transition of Si(111)(4x1)-in, Phys. Rev. Lett. 102 (2009) 115501, https://doi.org/10.1103/PhysRevLett.102.115501.

[126] S. Riikonen, A. Ayuela, D. Sánchez-Portal, Metal–insulator transition in the In/Si(111) surface, Surf. Sci. 600 (2006) 3821–3824, https://doi.org/10.1016/j.susc.2006.01.092.

[127] F. Klasing, Indium on Si(111) - Low-energy electron diffraction experiments and simulations on the striped (8x2) surface reconstruction and on the (4x1)<->(8x2) phase-transition, Universität Duisburg-Essen (2014).

[128] M.A. Van Hove, W.H. Weinberg, C.-M. Chan. Low-Energy Electron Diffraction: Experiment, Theory and Surface Structure Determination, Springer-Verlag, Berlin Heidelberg, 1986. https://www.springer.com/de/book/9783642827235.
[129] M.A. Van Hove, S.Y. Tong, Surface crystallography by LEED, Springer-Verlag, Berlin Heidelberg New York, 1979.
[130] J.M. Zuo, J.C.H. Spence, Advanced transmission electron microscopy, Springer Science+Business Media, New York, 2017.
[131] A. Feist, N. Bach, N. Rubiano da Silva, T. Danz, M. Möller, K.E. Priebe, T. Domröse, J.G. Gatzmann, S. Rost, J. Schauss, S. Strauch, R. Bormann, M. Sivis, S. Schäfer, C. Ropers, Ultrafast transmission electron microscopy using a laser-driven field emitter: Femtosecond resolution with a high coherence electron beam, Ultramicroscopy 176 (2017) 63–73, https://doi.org/10.1016/j.ultramic.2016.12.005.
[132] A. Hanisch-Blicharski, A. Janzen, B. Krenzer, S. Wall, F. Klasing, A. Kalus, T. Frigge, M. Kammler, M. Horn-von Hoegen, Ultra-fast electron diffraction at surfaces: From nanoscale heat transport to driven phase transitions, Ultramicroscopy 127 (2013) 2–8. https://doi.org/10.1016/j.ultramic.2012.07.017.
[133] G. Storeck, S. Vogelgesang, M. Sivis, S. Schäfer, C. Ropers, Nanotip-based photoelectron microgun for ultrafast LEED, Struct. Dyn. 4 (2017) 044024, https://doi.org/10.1063/1.4982947.
[134] B.J. Siwick, J.R. Dwyer, R.E. Jordan, R.J.D. Miller, Ultrafast electron optics: propagation dynamics of femtosecond electron packets, J. Appl. Phys. 92 (2002) 1643–1648, https://doi.org/10.1063/1.1487437.
[135] S. Vogelgesang, G. Storeck, J.G. Horstmann, T. Diekmann, M. Sivis, S. Schramm, K. Rossnagel, S. Schäfer, C. Ropers, Phase ordering of charge density waves traced by ultrafast low-energy electron diffraction, Nat. Phys. 14 (2018) 184–190, https://doi.org/10.1038/nphys4309.
[136] M. Gulde, S. Schweda, G. Storeck, M. Maiti, H.K. Yu, A.M. Wodtke, S. Schafer, C. Ropers, Ultrafast low-energy electron diffraction in transmission resolves polymer/graphene superstructure dynamics, Science 345 (2014) 200–204, https://doi.org/10.1126/science.1250658.
[137] G. Storeck, Non-equilibrium structural Dynamics of incommensurate Charge-Density Waves: Diffractive Probing with a micron-scale ultrafast Electron Gun, Georg-August-Universität Göttingen, 2020. https://ediss.uni-goettingen.de/handle/21.11130/00-1735-0000-0005-13F4-2.
[138] B. Wit, O. Bunjes, M. Wenderoth, C. Ropers, Structure and nonequilibrium heat-transfer of a Physisorbed Molecular layer on graphene, Adv. Mater. Interfaces 7 (2020) 2000473, https://doi.org/10.1002/admi.202000473.
[139] P. Buchsteiner, F. Sohn, J.G. Horstmann, J. Voigt, M. Ciomaga Hatnean, G. Balakrishnan, C. Ropers, P.E. Blöchl, M. Wenderoth, Surface resonance of the (2x1) reconstructed lanthanum hexaboride (001)-cleavage plane: a combined STM and DFT study, Phys. Rev. B 100 (2019) 205407, https://doi.org/10.1103/PhysRevB.100.205407.
[140] S. Wall, D. Wegkamp, L. Foglia, K. Appavoo, J. Nag, R.F. Haglund Jr, J. Stähler, M. Wolf, Ultrafast changes in lattice symmetry probed by coherent phonons, Nat. Commun. 3 (2012) 721, https://doi.org/10.1038/ncomms1719.
[141] S.D. Brorson, J.G. Fujimoto, E.P. Ippen, Femtosecond electronic heat-transport dynamics in thin gold films, Phys. Rev. Lett. 59 (1987) 1962–1965, https://doi.org/10.1103/PhysRevLett.59.1962.
[142] Y. Li, T.F. Heinz, Optical models for thin layers, arXiv:1801.00402 (2018). http://arxiv.org/abs/1801.00402.
[143] S. Chandola, K. Hinrichs, M. Gensch, N. Esser, S. Wippermann, W.G. Schmidt, F. Bechstedt, K. Fleischer, J.F. McGilp, Structure of Si(111)-in nanowires determined from the Midinfrared optical response, Phys. Rev. Lett. 102 (2009) 226805, https://doi.org/10.1103/PhysRevLett.102.226805.
[144] P. Puschnig, S. Berkebile, A.J. Fleming, G. Koller, K. Emtsev, T. Seyller, J.D. Riley, C. Ambrosch-Draxl, F.P. Netzer, M.G. Ramsey, Reconstruction of Molecular orbital densities from photoemission data, Science 326 (2009) 702–706, https://doi.org/10.1126/science.1176105.
[145] M. Born, R. Oppenheimer, Zur quantentheorie der molekeln, Ann. Phys. 389 (1927) 457–484, https://doi.org/10.1002/andp.19273892002.
[146] G.A. Garrett, T.F. Albrecht, J.F. Whitaker, R. Merlin, Coherent THz phonons driven by light pulses and the Sb problem: what is the mechanism? Phys. Rev. Lett. 77 (1996) 3661–3664, https://doi.org/10.1103/PhysRevLett.77.3661.
[147] T.E. Stevens, J. Kuhl, R. Merlin, Coherent phonon generation and the two stimulated raman tensors, Phys. Rev. B 65 (2002) 144304, https://doi.org/10.1103/PhysRevB.65.144304.
[148] L. Rettig, J.-H. Chu, I.R. Fisher, U. Bovensiepen, M. Wolf, Coherent dynamics of the charge density wave gap in tritellurides, Faraday Discuss. 171 (2014) 299–310, https://doi.org/10.1039/C4FD00045E.
[149] T. Huber, S.O. Mariager, A. Ferrer, H. Schäfer, J.A. Johnson, S. Grübel, A. Lübcke, L. Huber, T. Kubacka, C. Dornes, C. Laulhe, S. Ravy, G. Ingold, P. Beaud, J. Demsar, S.L. Johnson, Coherent structural dynamics of a prototypical Charge-density-wave-to-metal transition, Phys. Rev. Lett. 113 (2014) 026401, https://doi.org/10.1103/PhysRevLett.113.026401.
[150] Z. Wang, C. Chen, J. Mo, J. Zhou, K.P. Loh, Y.P. Feng, Decisive role of electron-phonon coupling for phonon and electron instabilities in transition metal dichalcogenides, Phys. Rev. Res. 5 (2023) 013218, https://doi.org/10.1103/PhysRevResearch.5.013218.
[151] M.J. Neugebauer, T. Huber, M. Savoini, E. Abreu, V. Esposito, M. Kubli, L. Rettig, E. Bothschafter, S. Grübel, T. Kubacka, J. Rittmann, G. Ingold, P. Beaud, D. Dominko, J. Demsar, S.L. Johnson, Optical control of vibrational coherence triggered by an ultrafast phase transition, Phys. Rev. B 99 (2019) 220302, https://doi.org/10.1103/PhysRevB.99.220302.
[152] H. Tanimura, J. Kanasaki, K. Tanimura, J. Sjakste, N. Vast, Ultrafast relaxation dynamics of highly excited hot electrons in silicon, Phys. Rev. B 100 (2019) 035201, https://doi.org/10.1103/PhysRevB.100.035201.
[153] D. Rosenthal, Functional surfaces in heterogeneous catalysis: a short review, Phys. Status Solidi A 208 (2011) 1217–1222, https://doi.org/10.1002/pssa.201001207.
[154] S.K. Song, A. Samad, S. Wippermann, H.W. Yeom, Dynamical metal to Charge-density-wave junctions in an atomic wire Array, Nano Lett. (2019), https://doi.org/10.1021/acs.nanolett.9b02438.
[155] T. Frigge. Ultraschnelle strukturelle Nichtgleichgewichtsdynamik des optisch angeregten Si(111)(8x2)→(4x1)-In Phasenübergangs, 2016. https://duepublico2.uni-due.de/receive/duepublico_mods_00041658.
[156] C.W. Nicholson. Electronic Structure and Dynamics of Quasi-One Dimensional Materials, Freie Universität Berlin, 2018. https://refubium.fu-berlin.de/handle/fub188/22174.
[157] J. Guo, G. Lee, E.W. Plummer, Intertwined electronic and structural phase transitions in the In/Si(111) Interface, Phys. Rev. Lett. 95 (2005) 046102, https://doi.org/10.1103/PhysRevLett.95.046102.
[158] V.R. Morrison, R.P. Chatelain, K.L. Tiwari, A. Hendaoui, A. Bruhács, M. Chaker, B.J. Siwick, A photoinduced metal-like phase of monoclinic VO_2 revealed by ultrafast electron diffraction, Science 346 (2014) 445–448, https://doi.org/10.1126/science.1253779.
[159] D.N. Basov, R.D. Averitt, D. Hsieh, Towards properties on demand in quantum materials, Nat. Mater. 16 (2017) 1077–1088, https://doi.org/10.1038/nmat5017.
[160] A. de la Torre, D.M. Kennes, M. Claassen, S. Gerber, J.W. McIver, M.A. Sentef, Colloquium: nonthermal pathways to ultrafast control in quantum materials, Rev. Mod. Phys. 93 (2021) 041002, https://doi.org/10.1103/RevModPhys.93.041002.
[161] T.F. Nova, A.S. Disa, M. Fechner, A. Cavalleri, Metastable ferroelectricity in optically strained $SrTiO_3$, Science 364 (2019) 1075–1079, https://doi.org/10.1126/science.aaw4911.
[162] A.S. Disa, J. Curtis, M. Fechner, A. Liu, A. von Hoegen, M. Först, T.F. Nova, P. Narang, A. Maljuk, A.V. Boris, B. Keimer, A. Cavalleri, Photo-induced high-temperature ferromagnetism in YTiO3, Nature 617 (2023) 73–78, https://doi.org/10.1038/s41586-023-05853-8.
[163] X. Li, T. Qiu, J. Zhang, E. Baldini, J. Lu, A.M. Rappe, K.A. Nelson, Terahertz field–induced ferroelectricity in quantum paraelectric $SrTiO_3$, Science 364 (2019) 1079–1082, https://doi.org/10.1126/science.aaw4913.
[164] A.H. Zewail, Femtochemistry: atomic-scale dynamics of the chemical bond, J. Phys. Chem. A 104 (2000) 5660–5694, https://doi.org/10.1021/jp001460h.
[165] E.D. Potter, J.L. Herek, S. Pedersen, Q. Liu, A.H. Zewail, Femtosecond laser control of a chemical reaction, Nature 355 (1992) 66, https://doi.org/10.1038/355066a0.
[166] M. Mitrano, A. Cantaluppi, D. Nicoletti, S. Kaiser, A. Perucchi, S. Lupi, P. Di Pietro, D. Pontiroli, M. Riccò, S.R. Clark, D. Jaksch, A. Cavalleri, Possible light-induced superconductivity in K_3C_{60} at high temperature, Nature 530 (2016) 461–464, https://doi.org/10.1038/nature16522.
[167] D. Fausti, R.I. Tobey, N. Dean, S. Kaiser, A. Dienst, M.C. Hoffmann, S. Pyon, T. Takayama, H. Takagi, A. Cavalleri, Light-induced superconductivity in a stripe-ordered cuprate, Science 331 (2011) 189–191, https://doi.org/10.1126/science.1197294.

[168] M. Rini, R. Tobey, N. Dean, J. Itatani, Y. Tomioka, Y. Tokura, R.W. Schoenlein, A. Cavalleri, Control of the electronic phase of a manganite by mode-selective vibrational excitation, Nature 449 (2007) 72–74, https://doi.org/10.1038/nature06119.
[169] A.M. Weiner, D.E. Leaird, G.P. Wiederrecht, K.A. Nelson, Femtosecond pulse sequences used for optical manipulation of molecular motion, Science 247 (1990) 1317–1319, https://doi.org/10.1126/science.247.4948.1317.
[170] K.A. Nelson, The prospects for impulsively driven, mode-selective chemistry in condensed phases, in: J. Jortner, R.D. Levine, B. Pullman (Eds.), Mode Sel. Chem., Springer Netherlands, 1991: pp. 527–533.
[171] T. Feurer, J.C. Vaughan, K.A. Nelson, Spatiotemporal coherent control of lattice vibrational waves, Science 299 (2003) 374–377, https://doi.org/10.1126/science.1078726.
[172] K. Ishioka, M. Hase, M. Kitajima, L. Wirtz, A. Rubio, H. Petek, Ultrafast electron-phonon decoupling in graphite, Phys. Rev. B 77 (2008) 121402, https://doi.org/10.1103/PhysRevB.77.121402.